34

Radiative Proton Capture to Second Harmonic Giant Dipole States in ^{13}N

by
Douw Steyn

A thesis submitted to the Faculty of Science
of the University of Cape Town for the
degree of Master of Science in
Physics.

March 1990

Abstract

Angular distributions have been measured for the radiative proton capture reaction $^{12}C(p,\gamma)^{13}N$ at beam energies from 40 to 54 MeV. Measurements were made with the new, large anticoincidence-shielded spectrometer *HAGAR* at angles from 30° to 150° to the beam direction. Differential and total cross-sections have been calculated from these data, and show evidence for resonant behaviour for the transitions to the ground state, the first excited state, and the unresolved second and third excited states. The total cross-sections for these transitions peak at a proton energy of about 46 MeV which is twice the centroid energy of the Giant Dipole Resonance (GDR) based on the ground state of ^{13}N.

Acknowledgements

I would like to express my sincere appreciation to the following people for their great help, without which this work would have been impossible.

- Professor D.G. Aschman, my supervisor, for his time and patience, and his willingness to discuss issues at any time. His encouragement and enthusiasm kept me going through many a frustrating period.
- Dr. A. Zucchiatti for sharing his extensive knowledge of this field of work with me, and for the many hours spent together on the experiment.
- Professor J.P.F. Sellschop and Dr. R. Fearick for their support and enthusiasm during the project.
- Mark Murray and Dr. John Pilcher for their computing expertise which was so valuable to this work, and for their friendly readiness to share it with me.
- Dr. D. Reitmann, the director of the National Accelerator Centre, and Dr. A.H. Botha and the technical staff for providing an excellent experimental environment.
- Professor F.D. Brooks and Dr. W.A. Cilliers, and all the postgraduates in the UCT Nuclear Physics Group for the stimulating discussions and infectious enthusiasm which rubbed off on me.
- The Foundation for Research Development of the CSIR for their financial support.

Contents

Chapter 1

Introduction

The giant multipole resonances are collective oscillations of high frequency and low amplitude of all the nucleons in the nucleus. They are states which have a large transition probability to single particle states. Schematically, they can be thought of as a coherent superposition of all possible particle-hole transitions of a given multipolarity and parity [Woud 87]. In the shell model they are characterized by transitions between oscillator shells; the number of shells over which the transition occurs, N, determining the multipolarity and the order of magnitude energy of the resonance $N\hbar\omega \sim 41A^{-1/3}$. The electric modes are distinguished from the magnetic modes by a lack of spin differentiation ($\Delta S = 0$), whereas the isovector modes differ from the isoscalar modes in that in the former the protons and neutrons move out of phase from each other ($\Delta T = 1$) while the latter have no isospin differentiation ($\Delta T = 0$).

The giant electric dipole resonance is explained as an out of phase oscillation between the protons and neutrons in the nucleus. One simple model of this resonance was given by Goldhaber and Teller [Gold 48] in which the neutrons and protons are described as classical, incompressible fluids which oscillate against each other with a restoring force proportional to the volume symmetry energy. This can be considered to be a standing wave inside a fixed spherical volume for which the wavelength λ equals the dimension of the nucleus R and so $E = h\nu = \hbar\omega \propto 1/\lambda = 1/R \propto A^{-1/3}$. An alternative picture, illustrated schematically in Figure 1.1, considers the oscillation of a proton sphere against a neutron sphere [Myer 74] where the restoring force is proportional to the surface symmetric energy, $E \propto A^{-1/6}$. Taking a superposition of these two modes leads to rough agreement of the centroid energy with experiment over a large range of nuclei with the empirical

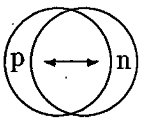

Figure 1.1: The isovector ($\Delta T = 1, \Delta S = 0$) E1 giant dipole resonance.

result [Berm 75] $E = 31.2A^{-1/3} + 20.6A^{-1/6}$ MeV. The electric dipole transitions occur between states of different parity such that $\pi = \pi_i \pi_f = -1$ and $|J_f - J_i| \leq L \leq J_f + J_i$.

Historically the giant dipole resonance was first observed with the photoabsorption reactions (γ,n) and (γ,p). The problem of obtaining good monochromatic photon beams at high energies led to the increasing use of the inverse (p,γ) reaction to study the GDR at higher energies. Such reactions have the advantage of good quality, monochromatic proton beams and high resolution gamma ray spectrometers to study the reaction products, and can be related to the photoabsorption reaction by detailed balance, at least in the ground state transition case. Initially the chief tool in this field was the tandem Van de Graaff accelerator and the favourite targets were nuclei such as ^{11}B because of the large Q-values of reactions like ^{11}B(p,γ)^{12}C where Q = 15.96 MeV. The use of high energy cyclotrons enabled the study of reactions such as ^{12}C(p,γ)^{13}N which has a Q-value of only 1.944 MeV and reactions which excited giant resonances based on excited states of the nucleus. In this regard the 200 MeV cyclotron at the NAC [Both 86] in Faure near Cape Town and the spectrometer *HAGAR* [Zucc 86] make an ideal combination for this type of work. According to the Brink hypothesis [Brin 55] one should observe giant resonances, and specifically giant dipole resonances, built not only on the ground state of the nucleus, but also on excited states. An extension of this hypothesis leads to the expectation that one should be able to detect the GDR built upon the GDR based on the ground state; the so-called 'second harmonic' of the GDR. Evidence for such second harmonic states has been reported by Blatt, Anghinolfi, Weller [Blat 84,Angh 82,Well 82] and others for a variety of nuclei including ^{12}C, ^{13}N and ^{28}Si. Most work in this field until recently has been restricted to the lower energy region. The work that has been published for beam energies of 40 MeV or higher is often restricted to one angle or energy and frequently does not report a measurement of the total cross section. The use of a carbon target to explore the highly excited states of ^{13}N has been done by Fisher *et* *al.* [Fish 63] ,for example, who report differential cross-sections at 90° to the beam direction for the transitions to the ground state and the unresolved second and third excited states (referred to as the γ_0 and γ_{2+3} transitions). An energy level diagram showing the low energy states of ^{13}N and the first few transitions is given in Figure 1.2. Blatt *et al.* [Blat 84] measured a full angular distribution for a range of energies but concentrated on the great similarities between the gamma spectra of the neighbouring nuclei ^{12}C and ^{13}N. Hausman also observed the reaction $^{12}C(\vec{p},\gamma)^{13}N$ at high beam energies [Haus 88] but report only a 60° point, although they publish an angular distribution for $E_p = 28.5\,\text{MeV}$. This latter work also represents a recent trend to use polarized proton beams for this sort of work. So the available data on ^{13}N in this region is far from complete, and this experiment is an attempt to fill some of the gaps.

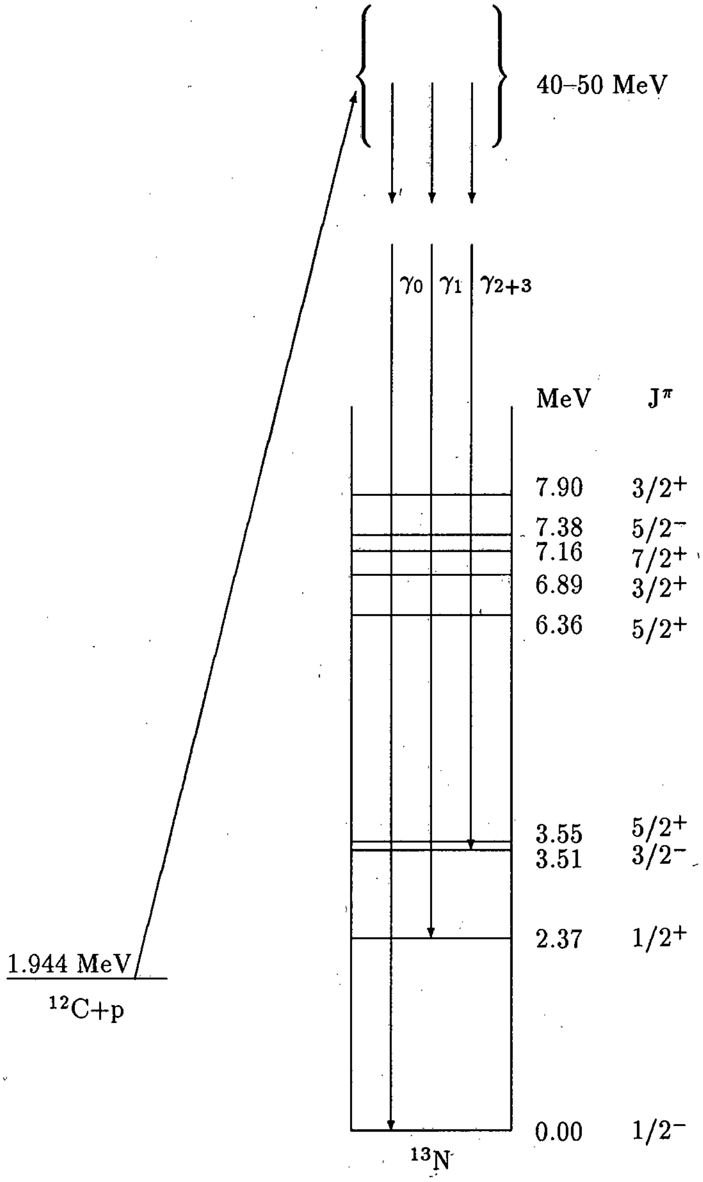

Figure 1.2: Transitions in the reaction $^{12}C(p,\gamma)^{13}N$. Note the break in the energy scale at about 11 MeV.

Chapter 2

Experimental Setup

2.1 The Spectrometer

The *High energy Anticoincidence GAmma Ray* spectrometer, named HAGAR (see Figures 2.1 and 2.2), consists of a large, central, surface compensated NaI(Tl) crystal grown from a single ingot [Zucc 86]. It is surrounded on the sides by a segmented shield, and in front by a disk, of plastic BC408 scintillator. These two plastic components are run in anticoincidence with the NaI detector to discriminate against escape events from the central detector as well as background events which include a significant cosmic contribution. A cylindrical lead shield and a front lead collimator surround the detectors. Borax blocks are stacked around the apparatus, including a borax plug inside the collimator, to further reduce the neutron background. The wax has a density of $0.85\,g/cm^3$ and is loaded with 15% – 20% borax by weight. The spectrometer views a solid angle of 19.2 msr with a collection angle of approximately 4.5°. The collimation angle is set so that the entire back surface of the crystal sees the target, while the collection angle is small enough to maintain good angular resolution. The front surface of the NaI crystal is fixed at 120 cm from the target in order to achieve distinct time separation of neutrons and photons for time-of-flight discrimination.

The NaI(Tl) crystal, manufactured by Bicron, is viewed by seven RCA 4900 7.6 cm photomultipliers with voltage stabilised bases to prevent gain drifts (see for example reference [Ohmo 87] for an investigation of their performance), the outputs of which are passively mixed. The annulus of plastic scintillator (BC408) is divided into six optically separated segments, ensuring better light collection and resolution. Each of these segments is viewed by two Amperex XP-2202 5 cm photomultipliers. The front plastic disk is

Element	Inner radius (cm)	Outer radius (cm)	Length (cm)	Distance from target (cm)	Tangent of inner taper angle
Target		0.75	0.01		
NaI(Tl)		11.9	35.6	120.0	
NE110 (annulus)	14.4	24.3	61.0	118.0	
NE110 (front disk)		24.3	8.0	108.0	
Lead (annulus)	29.0	39.5	84.0	104.0	
Lead (collimator)	6.3	34.5	24.0	80.0	0.0729
Borax shield	42.5	72.5	170.0	60.0	
Borax plug		6.3	30.0	70.0	

Table 2.1: Design parameters of the spectrometer HAGAR

viewed by three XP-2202 photomultipliers placed at the side of the disk and at 120° from each other.

The spectrometer is mounted on a rotating platform which is pivoted around a point directly below the target. Due to the large size and weight of the spectrometer, the platform is lifted by four compressed air pads when the angle of observation is to be changed. The detector angle can be selected to within a few tenths of a degree in the range 30° to 150°. At these extreme angles the large volume of wax shielding comes into physical contact with the beamline, thus preventing observations at angles closer to the beam. Our targets were positioned on a target ladder which has place for five targets. The target chamber is mounted in the beam pipe and has perspex windows to allow the use of a video camera for beam focusing and alignment and to minimise the photon absorption by the walls of the chamber.

The design parameters of this detector were investigated and optimised [Zucc 86] with the use of a Monte Carlo computer code [Corv 81,Taiu 83] which simulates the progress of a photon inside the detector, taking into account all the processes to which it may be subjected. The final parameters used when building the spectrometer are summarized in Table 2.1. The Monte Carlo code assumes all elements of the detector to be cylindrical. Therefore, the lead collimator (see Figure 2.1) and the borax shield were assumed to be cylindrical for the calculations whereas, in fact, the true shape was more rectangular while the front lead collimator was tapered externally as well as internally. The approximation is, however, believed to be a good one.

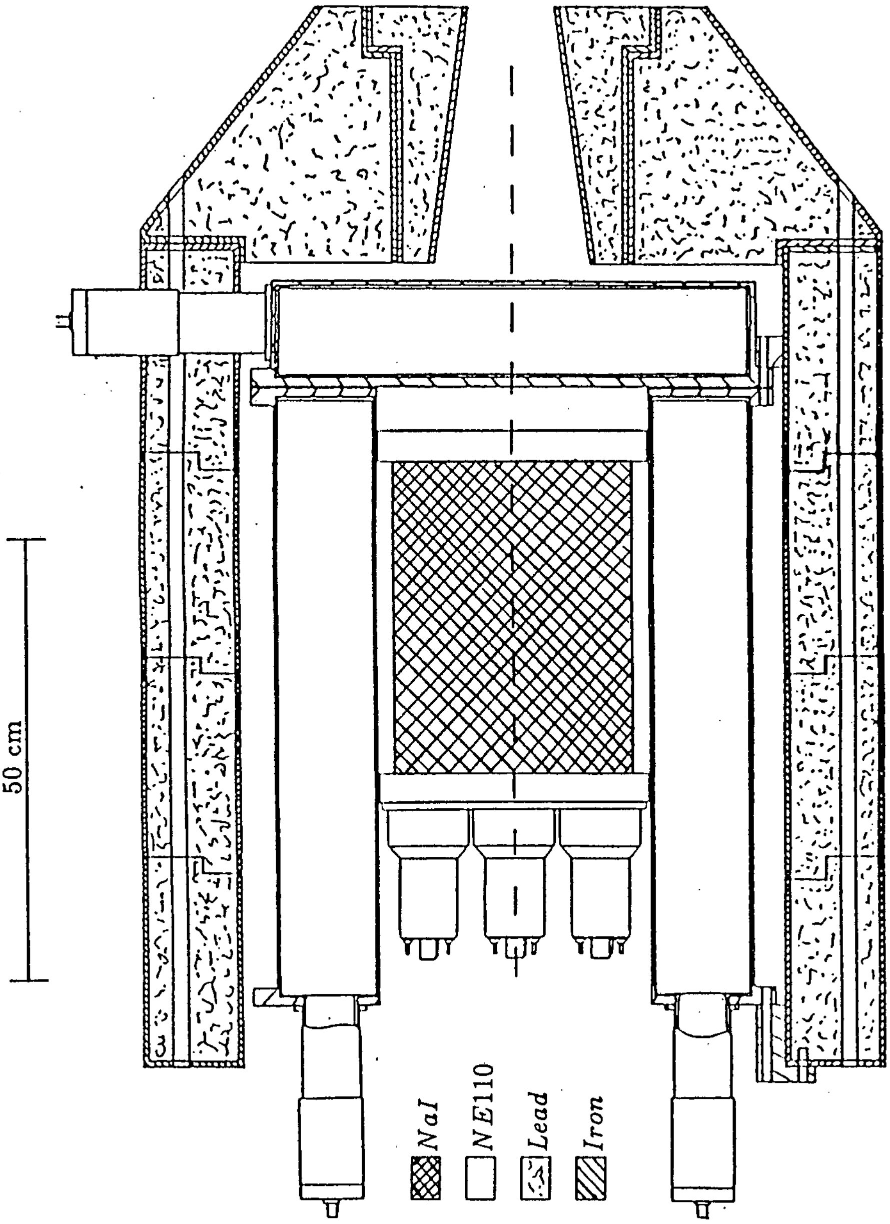

Figure 2.1: The gamma-ray spectrometer *HAGAR*.

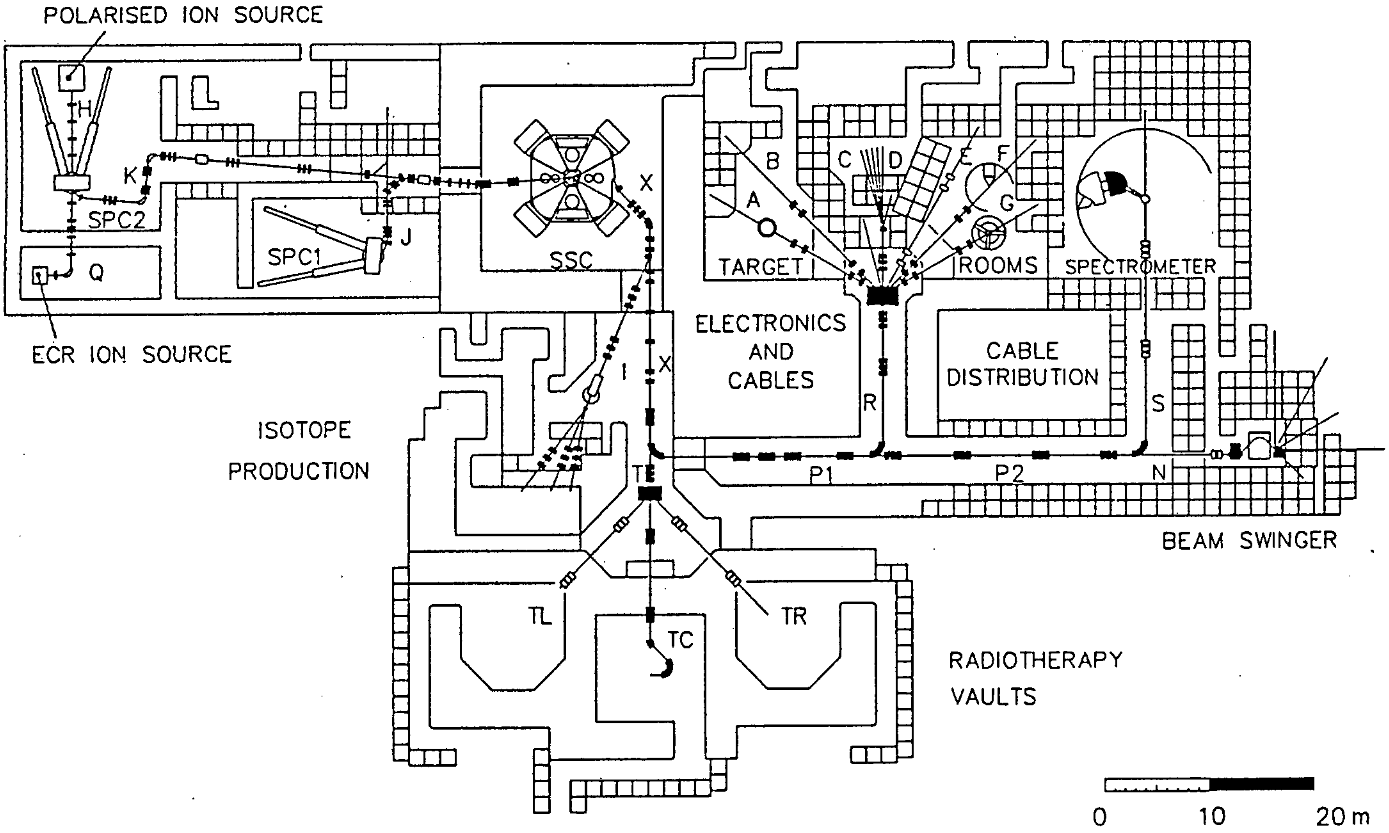

Figure 2.2: The layout of the 200 MeV cyclotron at the National Accelerator Centre (NAC) at Faure in South Africa, with the spectrometer *HAGAR* on beamline F.

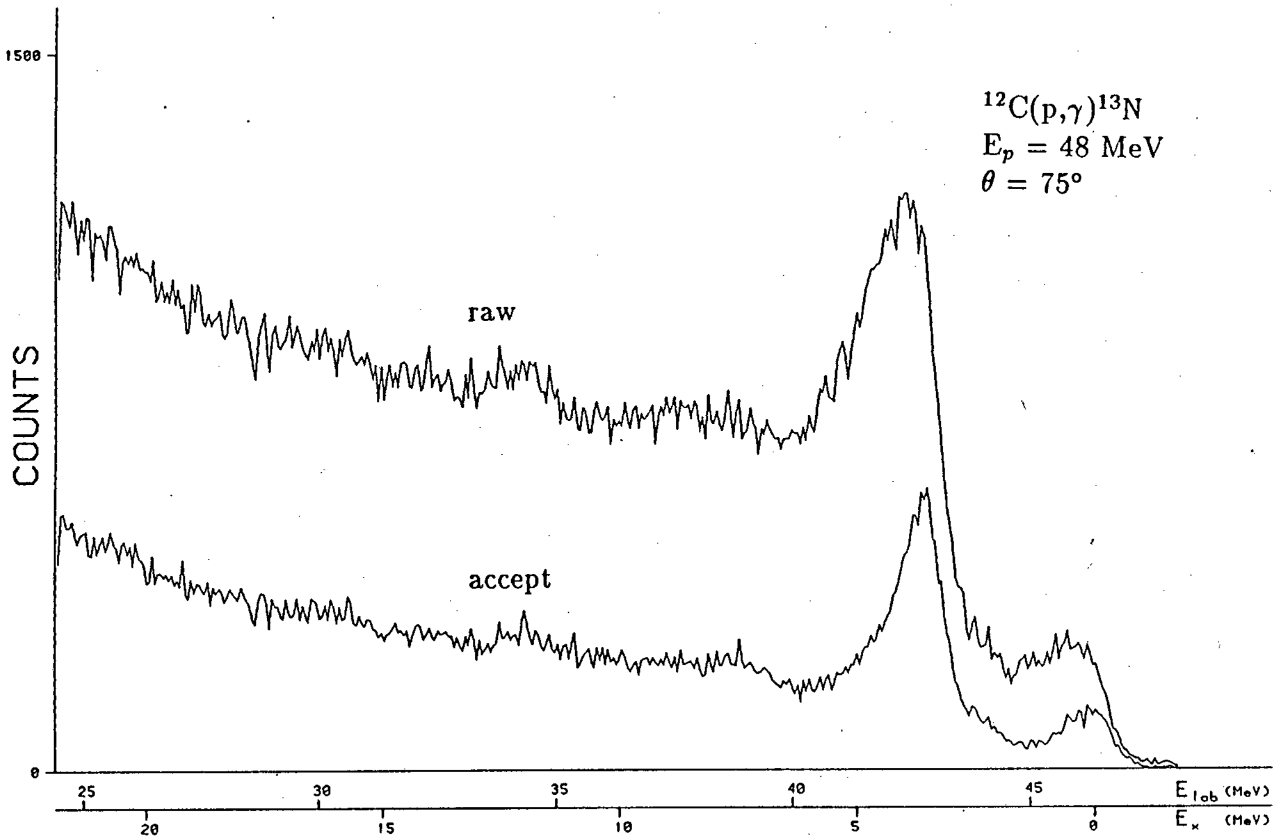

Figure 2.3: An example of a raw and accepted gamma spectrum, illustrating gamma rejection.

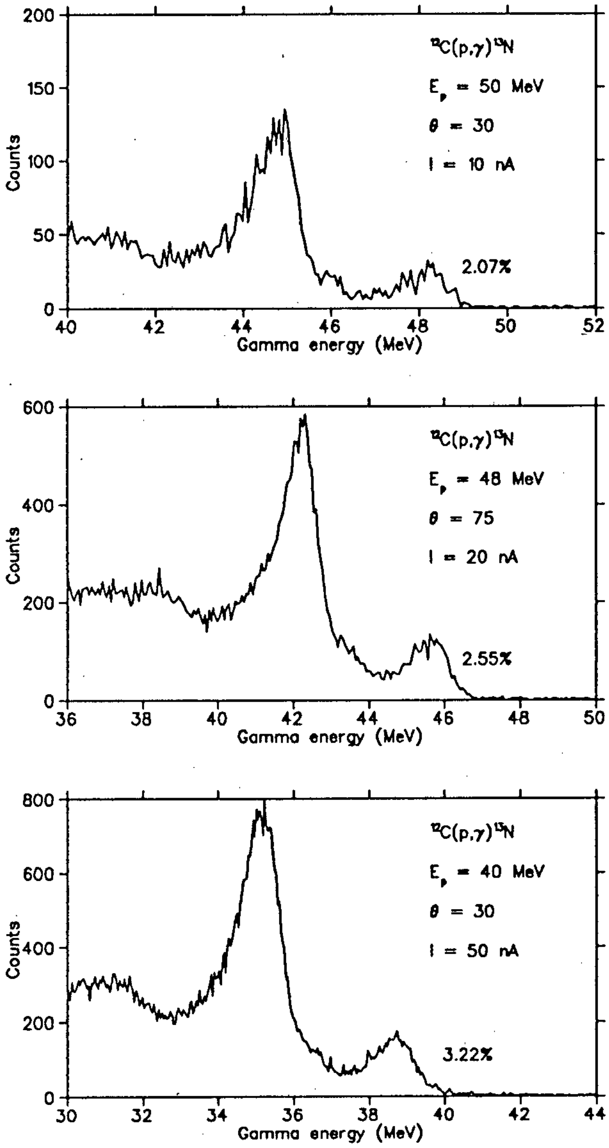

Figure 2.4: Some examples of detector resolution at high gamma energies. The two prominent peaks are the transitions to the ground state and the unresolved second and third excited states of ^{13}N, and the quoted percentages are the FWHM resolutions of the ground state peaks. Note the decrease in resolution with increasing beam current (I).

2.2 Data Acquisition

Data was acquired for nine different beam energies: 27, 40, 43.2, 46, 48, 49, 50, 52.5, and 54 MeV between April 1987 and February 1988. At each beam energy an angular distribution was measured with at least six points per distribution. Beam energy resolution was good with an uncertainty of less than 1 MeV. The beam pulses were well defined and separated; the separation ranging from 62 ns at Ep = 66 MeV to 72 ns at Ep = 44 MeV. On the target the beam was confined to a spot whose diameter varied between 0.5 cm and 1.5 cm. This was about half the total area of the target and thus no problems of beam on the target frame were encountered. A current integrator (Brookhaven Instruments BIC model 1000C) was used to measure the accumulated charge deposited by the proton beam in the beam dump. This was interfaced to the acquisition computer so that the integrated current for each run could be read automatically. Charges of 100 μC to 2500 μC were accumulated during the various runs while the beam currents varied between 3 nA and 50 nA.

The rejection of unwanted events was done electronically, with subsections of our electronics for the anticoincidence shield, the neutron time-of-flight discrimination, and pulse pileup handling. These are described in more detail in section 2.3. Figure 2.3 illustrates the rejection of unwanted events by comparing a raw gamma spectrum with an accepted gamma spectrum on the same axes.

The detector resolution at high photon energies was always less than 4%. Figure 2.4 shows a few examples with FWHM values for the ground state peak. It was noticed that a dramatic reduction in gamma energy resolution was observed when the beam current rose above ~15 nA. This was presumably due to pileup effects as evidenced by a peak of constant gamma energy of about 19.5 MeV which is unfortunately present in many of our spectra and is believed to be due to pileup of the 15.11 MeV and 4.4 MeV photons from the reaction ^{12}C(p,p$'$)^{12}C*. Acquisition of data was done on an online VAX 730 computer and the data were stored on disk and magnetic tape for later offline analysis on a VAX 750 and a VAX 6230. The acquisition and analysis program, XSYS, was originally developed at the Triangle Universities Nuclear Laboratory (TUNL) [Goul 81,Goul 83] and extensively modified at the Indiana University Cyclotron Facility (IUCF) [IUCF 84]. The program was further modified at the NAC [Pilc 89] to suit the particular requirements of that institution. This program was used for the acquisition of data and in conjunction with our own software for later analysis. A log of our runs is presented in Table 2.2. Some of our earlier runs were acquired with a resolution of 1 μC on the current integrator. This was changed during the experiment to 1 nC and is reflected in the log in the increased accuracy of the accumulated charge entry.

Run	E_p (MeV)	Detector angle, θ_{Lab} (degrees)	Target angle, ϕ (degrees)	Acc. Charge, Q (μC)	Beam current (nA)
C4030240	40.0	30.0	45.0	779	50
C4045243	40.0	45.0	45.0	1001	55
C4060241	40.0	60.0	45.0	794	50
C4060251	40.0	60.0	45.0	1351	50
C4075249	40.0	75.0	45.0	2650	50
C4075250	40.0	75.0	45.0	1003	50
C4090242	40.0	90.0	45.0	1004	50
C40A5244	40.0	105.0	45.0	1400	50
C40C0245	40.0	120.0	0.0	1851	50
C40C0248	40.0	120.0	0.0	2650	50
C40E8247	40.0	148.0	0.0	1802	50
C45M130A23	43.2	30.0	30.0	312	25
C45M145A26	43.2	45.0	30.0	329	25
C45M245A26	43.2	45.0	30.0	42	25
C45M160A23	43.2	60.0	30.0	192	25
C45M260A23	43.2	60.0	30.0	60	25
C45M360A23	43.2	60.0	30.0	270	25
C45M160A26	43.2	60.0	30.0	9	25
C45M260A26	43.2	60.0	30.0	245	25
C45M560A26	43.2	60.0	30.0	297	20
C45M660A27	43.2	60.0	30.0	17	20
C45M760A27	43.2	60.0	30.0	273	40
C45M175A26	43.2	75.0	30.0	255	25
C45M190A24	43.2	90.0	30.0	280	25
C45M1A5A25	43.2	105.0	30.0	354	25
C45M1C0A25	43.2	120.0	30.0	396	22
C45M1D6A24	43.2	136.0	30.0	389	25
C45M2E8A25	43.2	148.0	30.0	448	23
C45M3E8A25	43.2	148.0	30.0	9	20
C45M4E8A25	43.2	148.0	30.0	30	25
C4630235	46.0	30.0	0.0	652	55
C4630239	46.0	30.0	45.0	935	52
C4645234	46.0	45.0	0.0	653	50
C4660225	46.0	60.0	45.0	654	56
C4660236	46.0	60.0	45.0	959	53
C4675228	46.0	75.0	45.0	373	53
C4675229	46.0	75.0	45.0	647	55
C4690226	46.0	90.0	45.0	682	55
C4690238	46.0	90.0	45.0	1054	54
C46A5233	46.0	105.0	0.0	650	53
C46B5232	46.0	115.0	0.0	78	53
C46C0227	46.0	120.0	45.0	685	53

Table 2.2: Log of experimental runs.

Run	E_p (MeV)	Detector angle, θ_{Lab} (degrees)	Target angle, ϕ (degrees)	Acc. Charge, Q (μC)	Beam current (nA)
C46D5230	46.0	135.0	0.0	651	50
C46E8231	46.0	148.0	0.0	651	50
C4830358	48.0	30.0	45.0	300.976	19
C4830359	48.0	30.0	45.0	1.035	5
C4845365	48.0	45.0	45.0	453.484	20
C4845366	48.0	45.0	45.0	1.099	5
C4860355	48.0	60.0	45.0	363.552	20
C4860357	48.0	60.0	45.0	0.559	5
C4860372	48.0	60.0	45.0	256.901	20
C4875363	48.0	75.0	45.0	1.524	5
C4875364	48.0	75.0	45.0	435.712	20
C4890353	48.0	90.0	45.0	1.275	20
C4890354	48.0	90.0	45.0	398.898	20
C48A5367	48.0	105.0	45.0	1.237	5
C48A5368	48.0	105.0	45.0	448.277	20
C48C0360	48.0	120.0	45.0	45.049	20
C48C0361	48.0	120.0	45.0	449.984	20
C48C0362	48.0	120.0	45.0	1.198	5
C48D5369	48.0	135.0	0.0	76.882	20
C48D5370	48.0	135.0	0.0	346.327	20
C48D5371	48.0	135.0	0.0	1.597	5
C48E7351	48.0	147.0	0.0	416.840	20
C48E7352	48.0	147.0	0.0	1.811	10
C4930223	49.0	30.0	45.0	566	50
C4945221	49.0	45.0	45.0	415	45
C4960216	49.0	60.0	45.0	90	20
C4960217	49.0	60.0	45.0	302	44
C4960224	49.0	60.0	45.0	3	10
C4990218	49.0	90.0	45.0	593	50
C49A0219	49.0	120.0	45.0	775	50
C49D5220	49.0	135.0	0.0	379	48
C5030347	50.0	30.0	45.0	0.956	3
C5030348	50.0	30.0	45.0	111.176	10
C5046378	50.0	46.0	45.0	408.728	20
C5046379	50.0	46.0	45.0	1.042	5
C5060341	50.0	60.0	45.0	8.224	11
C5060342	50.0	60.0	45.0	146.380	11
C5060343	50.0	60.0	45.0	1.463	3
C5060376	50.0	60.0	45.0	195.842	20
C5090344	50.0	90.0	45.0	316.460	10
C50C0345	50.0	120.0	45.0	224.497	11
C50C0346	50.0	120.0	45.0	1.029	3

Table 2.2: continued

Run	E_p (MeV)	Detector angle, θ_{Lab} (degrees)	Target angle, ϕ (degrees)	Acc. Charge, Q (μC)	Beam current (nA)
C50D5380	50.0	135.0	90.0	65.155	20
C50E7349	50.0	147.0	0.0	1.271	3
C50E7350	50.0	147.0	0.0	169.688	10
C5230208	52.5	30.0	45.0	240	15
C5230209	52.5	30.0	45.0	63	15
C5230210	52.5	30.0	45.0	131	12
C5245205	52.5	45.0	45.0	323	21
C5260201	52.5	60.0	45.0	360	15
C5275204	52.5	75.0	45.0	293	21
C5290202	52.5	90.0	45.0	208	13
C52A0203	52.5	120.0	45.0	205	12
C52D5206	52.5	135.0	0.0	378	20
C52E8207	52.5	148.0	0.0	432	21
C5431322	54.0	31.0	45.0	153.220	15
C5431323	54.0	31.0	45.0	1.001	3
C5445328	54.0	45.0	45.0	223.185	15
C5445329	54.0	45.0	45.0	0.742	3
C5445330	54.0	45.0	45.0	0.719	3
C5460318	54.0	60.0	45.0	89.890	15
C5460320	54.0	60.0	45.0	152.270	15
C5460321	54.0	60.0	45.0	1.160	3
C5475331	54.0	75.0	45.0	234.322	15
C5475332	54.0	75.0	45.0	1.114	3
C5490311	54.0	90.0	45.0	308	60
C5490312	54.0	90.0	45.0	155	30
C5490313	54.0	90.0	45.0	249	15
C5490314	54.0	90.0	45.0	222	15
C5490315	54.0	90.0	45.0	141	15
C5490317	54.0	90.0	45.0	3061	3
C54A5333	54.0	105.0	45.0	102.758	15
C54A5334	54.0	105.0	45.0	303.981	10
C54A5335	54.0	105.0	45.0	28.396	10
C54A5336	54.0	105.0	45.0	0.736	3
C54C0324	54.0	120.0	45.0	100.254	15
C54C0325	54.0	120.0	45.0	138.784	15
C54C0326	54.0	120.0	45.0	206.833	15
C54C0327	54.0	120.0	45.0	1.181	3
C54C0337	54.0	120.0	45.0	99.776	10
C54C0338	54.0	120.0	45.0	0.738	3
C54E8339	54.0	148.0	0.0	0.732	3
C54E8340	54.0	148.0	0.0	161.355	10

Table 2.2: continued

Our target ladder had place for five targets. These were occupied by a ceramic target for the checking of beam alignment and focusing, a boron target, the carbon target, a fluorine target, and an empty target frame for the determination of background. Almost no structure was seen in the fluorine spectra, so very little data were acquired for this target. The boron target was included as a check on our detector's performance since much published data on this target exists. It also provided one way of arriving at a suitable response function for the detector, since the transition to the two lowest lying states of carbon are manifest as two clean, well separated peaks. Thus almost all of our data were acquired with the carbon target. The boron target consists of a compressed boron powder of density 3.2 mg/cm^2. The carbon target was a double layer of solid polyethylene (CH_2) of density 15.85 mg/cm^2. Thus for a double layer it is 31.70 mg/cm^2. The angle of the target to the beam direction was varied depending on the detector angle. Three target angles were used, namely 0°, 30°, and 45° giving effective target densities of 31.70, 36.60, and 44.83 mg/cm^2 respectively. Energy loss in the carbon target varied between 0.34 MeV at Ep = 66 MeV and target angle of 0°, and 0.72 MeV at Ep = 40 MeV and target angle of 45°. An attempt was also made to determine the response function from the spectrum of a deuterium gas target, since this will contain one single, clear peak with very little background. Unfortunately, bad design of the gas cell prevented its use, and this procedure will have to wait for the cell to be redesigned.

An important factor in the determination of the detector efficiency and resolution is the setting of the threshold of the plastic anticoincidence shield. This is the lower energy limit at which the plastics will veto an event. Obviously, the lower the threshold the more events will be vetoed and the lower the efficiency of the detector. However, at the same time, fewer escape events will be seen and the resolution will be improved. A balance between the two must be found with the threshold dropping as the gamma energy increases, since at higher energies the peak resolution is the limiting factor of the detector performance. It is, however, very difficult to calibrate the plastic scintillators and, consequently, to determine the threshold accurately. As a result, unfortunately, too little attention was paid to this detail during the course of the experiment and the threshold was allowed to vary between 30 keV and about 200 keV as the beam energy decreased with little note being made of its value in the log book. Consequently, there is large uncertainty in its value at any time and in the correct response function to apply to the data. The solution to this problem is presented in section 3.2. Table 2.3 presents the detector efficiencies predicted by the Monte Carlo

E_γ	Anticoincidence threshold (keV)									
(MeV)	10	20	50	60	80	100	120	150	200	300
10	.228	.231	.239	.241	.245	.250	.255	.262	.273	.294
15	.224	.227	.235	.238	.244	.250	.256	.265	.281	.309
20	.215	.218	.228	.231	.238	.244	.251	.261	.277	.308
25	.197	.201	.211	.214	.221	.227	.235	.245	.261	.301
30	.191	.195	.206	.209	.216	.224	.231	.242	.262	.302
35	.178	.180	.190	.194	.200	.207	.215	.226	.245	.283
40	.164	.168	.179	.183	.190	.198	.205	.215	.236	.276
45	.155	.159	.169	.173	.180	.188	.195	.206	.224	.266
50	.149	.153	.164	.166	.173	.179	.186	.196	.218	.260
55	.135	.139	.149	.152	.158	.165	.171	.182	.202	.245
60	.130	.133	.142	.144	.151	.159	.166	.176	.195	.233

Table 2.3: The detector efficiencies predicted by the Monte Carlo simulation for various photon energies and detector anticoincidence thresholds. The efficiency is defined as the number of accepted events divided by the total number of events in the solid angle.

program for various photon energies and anticoincidence thresholds.

2.3 The Electronics

The electronic circuitry is shown in figure 2.6. The circuit may be split up into five main logical sections which, although not electronically independent of each other, fulfill different functions. Simplified, schematic diagrams of these sections are presented in figures 2.7 to 2.11. The simplifications include, for example, the omission of Le Croy 429A Logic Fan Outs which were often used when multiple loads had to be driven from a single output. The five components are described in detail below.

2.3.1 The NaI pulse handling

The pulses from the seven photomultiplier tubes viewing the NaI crystal are passively mixed (see figure 2.7), then fed through an attenuator box and a delay loop before entering the ADC interfaced to the acquisition computer. The delay loop is incorporated into the circuit in order to make the pulses coincident with the ADC gate pulses. The attenuator is used to reduce the amplitude of the pulses to the ADC. Further control is achieved by varying the width of the gate to the pulse integrating ADC.

2.3.2 The event trigger

We wished to observe any NaI pulse whose amplitude is greater than a certain threshold, ie. corresponding to a photon above a certain energy entering the NaI crystal. We have used an Ortec 584 constant fraction discriminator with its threshold set appropriately to provide a logic pulse whenever such an event occurs (see figure 2.8). This signal is fed through a Le Croy 821 quad discriminator since this module accepts a veto pulse and can thus be used to prevent multiple triggering while the computer is processing the first signal. The event signal from the Le Croy 821 discriminator is given to an Ortec 416A gate and delay generator which gives the event trigger signal to the computer interface and provides a strobe pulse to the NIM input register.The Le Croy 821 discriminator also provides, through another Ortec 416A gate and delay generator (GDG) and another Le Croy 821 discriminator, the gate for the ADC reading the NaI pulses. This is done because the Le Croy 821 discriminator has a convenient width range.

2.3.3 The plastic veto shield

The NaI and plastic scintillator signals whose amplitudes are greater than the thresholds set by their respective constant fraction discriminators are fed into a Le Croy 365AL four-fold logic unit (see figure 2.9). The plastic scintillator signals are first fed through a delay to align the coincidences correctly and a quad discriminator which is used to set the resolving time for the two pulses to be considered to be in coincidence. The logic unit produces a pulse when its two inputs are in coincidence, ie. when an event was observed in both the NaI and the plastic scintillators. This can happen when a cosmic ray passes through the detector or when an escape event from the NaI occurs. The $\gamma\gamma$-coincidence pulse is passed through an Ortec 416A gate and delay generator (GDG) before going in to the NIM input register in order for it to be read by the register at the correct time relative to the NIM strobe.

2.3.4 The neutron time-of-flight rejection

An Ortec 567 time-to-amplitude converter (TAC) is used to measure the time of flight of the reaction products from the target to the detector (see figure 2.10). The start pulse is taken from the Le Croy 821 'EVENT' discriminator. The stop pulse is generated from the cyclotron RF signal by passing it through an Ortec 436 100 MHz discriminator. It is also passed through a delay in order to bring the measured time of flight within the TAC range of 50 ns. The RF signal is used as a stop signal instead of the start signal in order to have more stop signals than starts to the TAC. The TAC output is fed to an ADC where it is read by the computer and displayed in a spectrum as a monitor on the condition of the experiment. Of importance to the rejection of neutrons is the TAC window which is set on the gamma peak. The SCA output from the TAC, which goes high whenever an event falls within the window, is fed through a level adapter to the NIM input register. The acquisition software then checks this channel in deciding whether to reject or accept an event. A second TAC is also present with the same inputs and its window set on the background next to the gamma peak. Only the SCA output from this TAC is viewed and it is used only as a monitor on the background. Figure 2.5 is an example of a time-of-flight spectrum which shows the effectiveness of this method of neutron rejection.

2.3.5 Pileup rejection

The NaI signal is fed from the timing filter amplifier to two constant fraction discriminators with different threshold settings (see figure 2.11). The threshold of the 'HIGH' CFD was set to approximately 14 MeV while that of the 'LOW' CFD was set to about 100 keV. The higher threshold is used to confine observations to the high energy region of interest, while the lower threshold cuts out electronic noise. By feeding the output from the 'LOW' CFD through a pileup inspector (PUI) to the NIM input register, the acquisition software could tell whether pileup of low pulses had occurred (referred to as LOLO), and reject the reading. Similarly the output from the 'HIGH' CFD passes through another PUI to the NIM input register to discriminate against pileup of high pulses (referred to as HIHI pileup). The rejection of pileup of high and low pulses is slightly more complicated. A 'LOW ONLY' signal was generated by putting the 'HIGH' CFD signal in anticoincidence with the 'LOW' CFD signal. This was achieved by putting the compliment of the 'HIGH' CFD signal in coincidence with the 'LOW' CFD signal at a Le Croy 365AL logic unit. Output from this unit then indicated a pulse in the range 100 keV to 14 MeV. This output was put in coincidence with the output from the 'HIGH' CFD signal at another 365AL logic unit to indicate whether pileup of a low and a high pulse had occurred. The Le Croy 222

Dual Gate Generator is a module containing two separate gate generators, so the 'LOW ONLY' and 'HIGH' signals are passed independently through gate generators to set the window in which overlaps are looked for. The signals are made wide enough so that an overlap of two pulses in which the 'HIGH' pulse comes first is also detected despite the 'HIGH' signal being delayed after the Le Croy 429 Fan Out. An Ortec 416A gate and delay generator (GDG) was used just before the final signal was sent to the NIM input register in order to time the signal correctly relative to the NIM strobe.

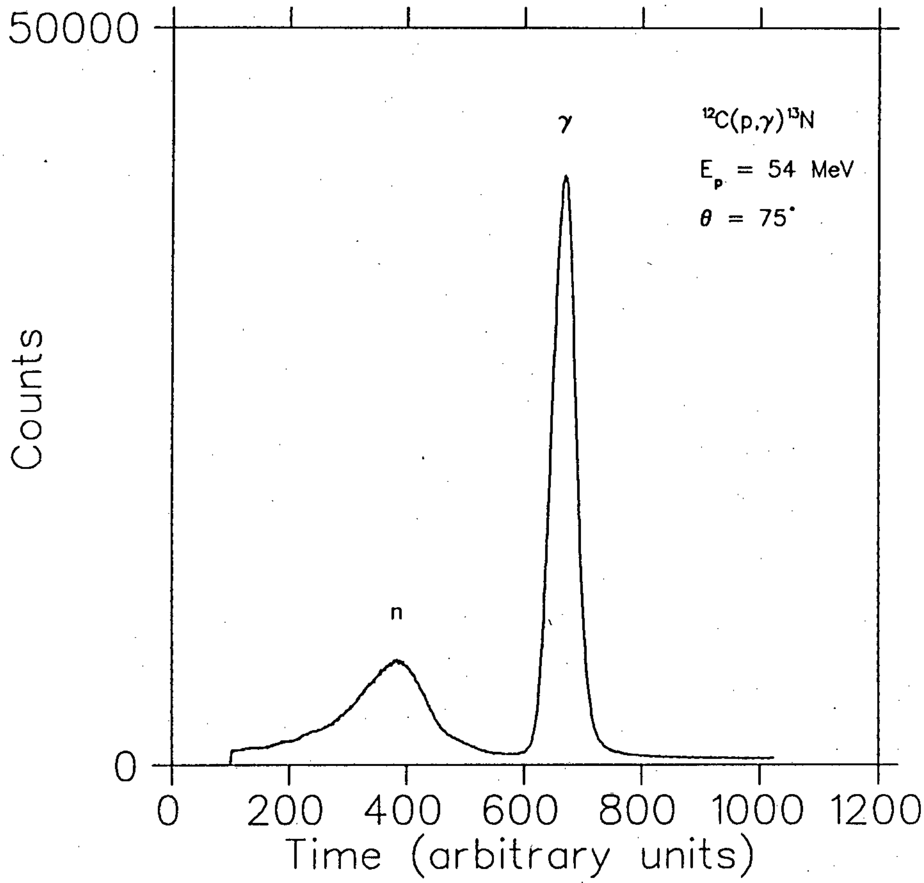

Figure 2.5: A time-of-flight spectrum showing the good separation of the gamma and neutron peaks and the low background.

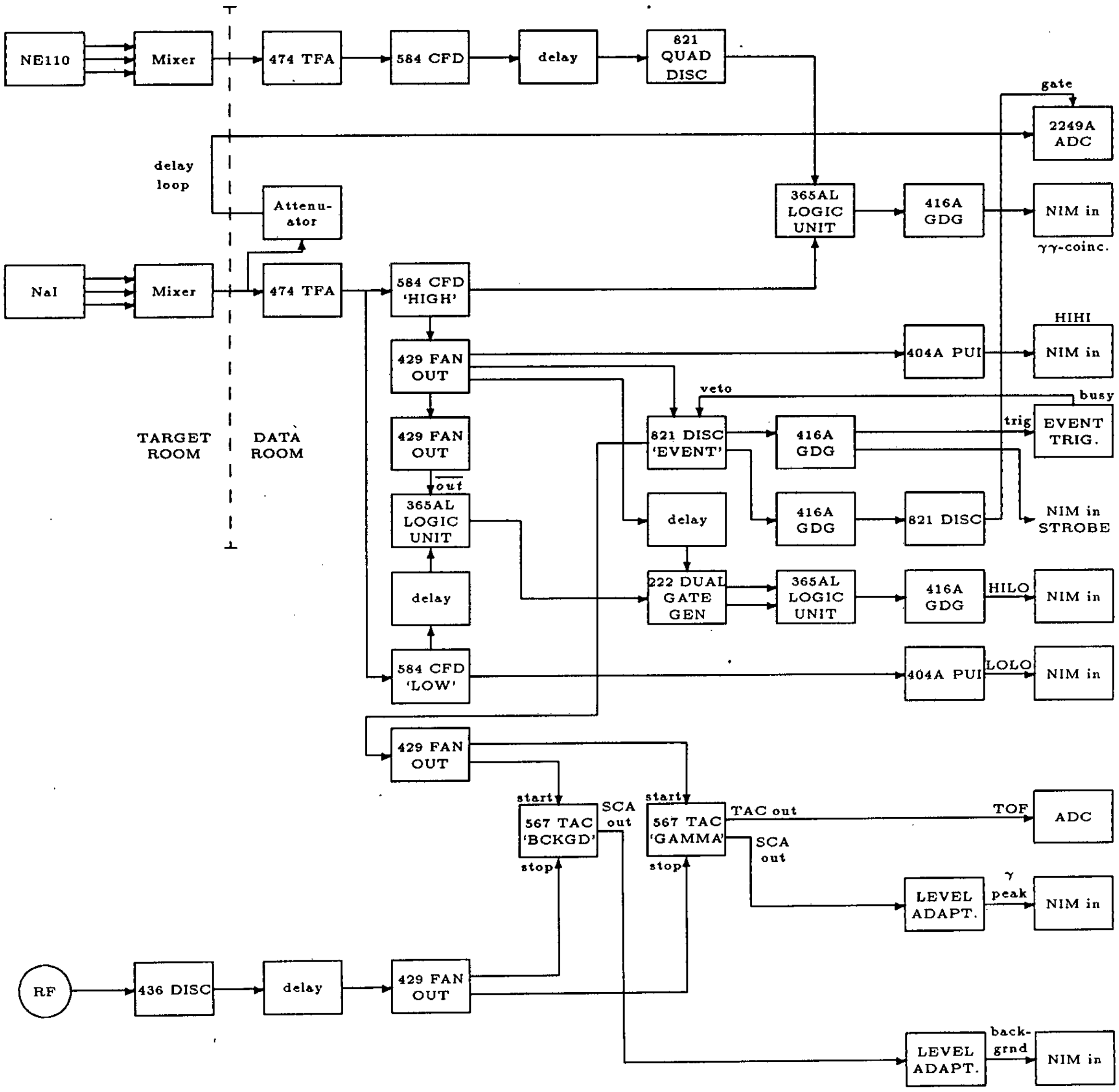

Figure 2.6: Electronics for the spectrometer HAGAR

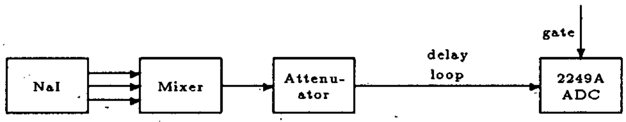

Figure 2.7: The NaI pulse handling.

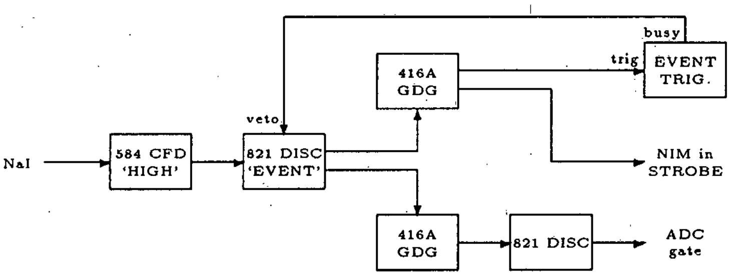

Figure 2.8: The event trigger.

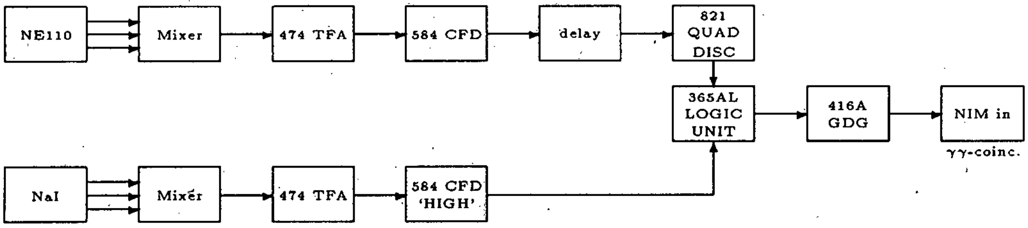

Figure 2.9: The plastic veto shield.

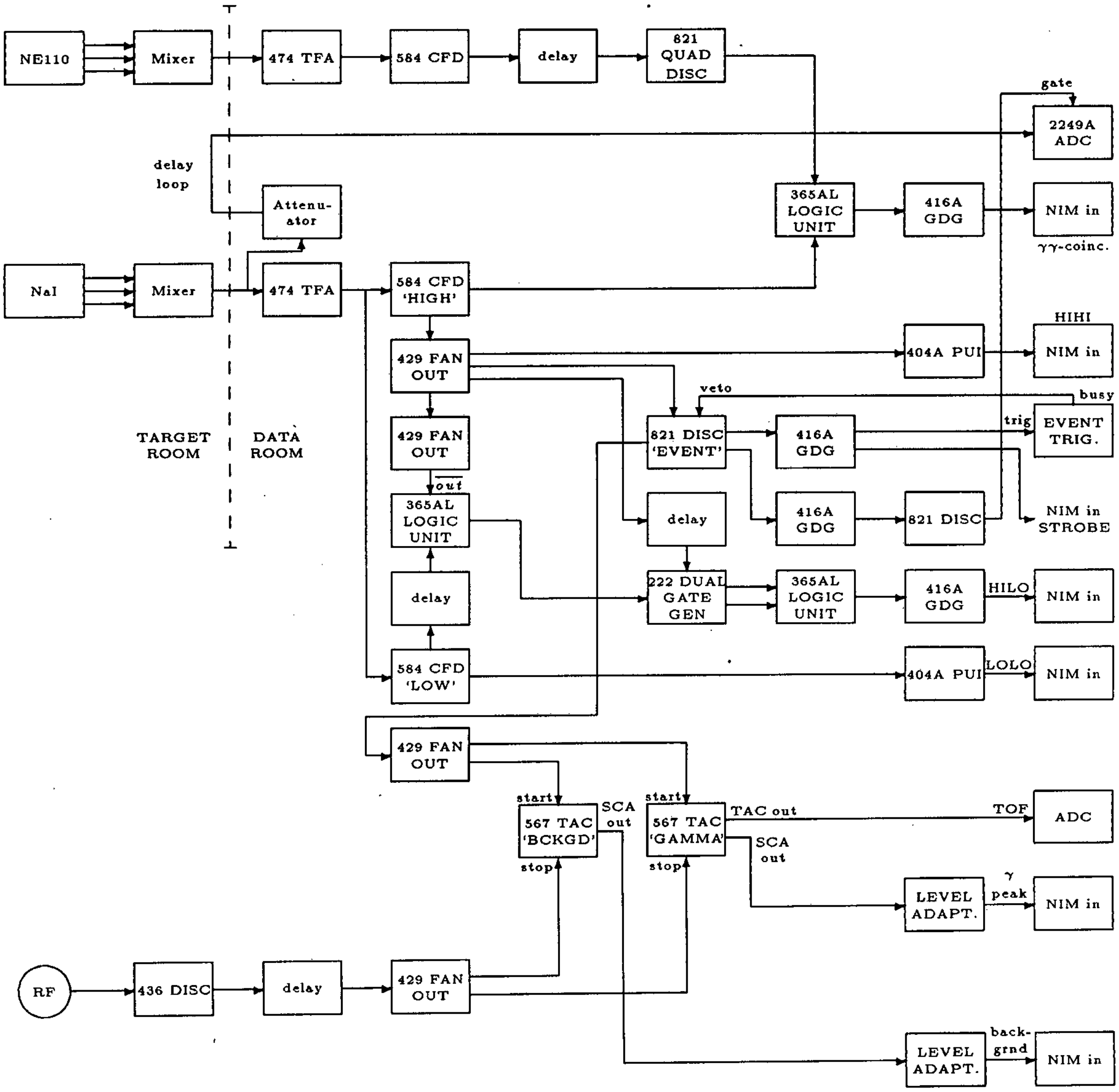

Figure 2.6: Electronics for the spectrometer HAGAR

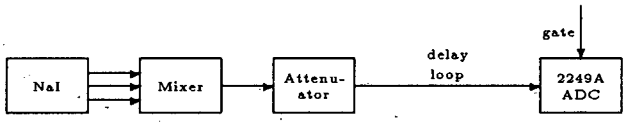

Figure 2.7: The NaI pulse handling.

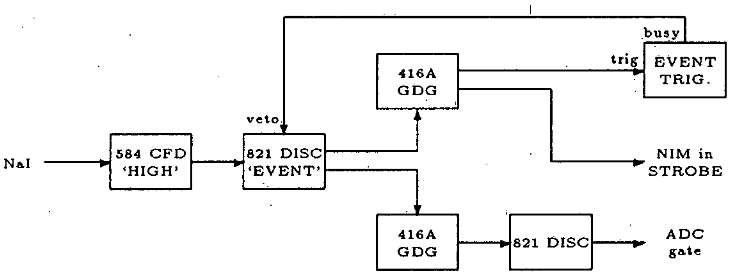

Figure 2.8: The event trigger.

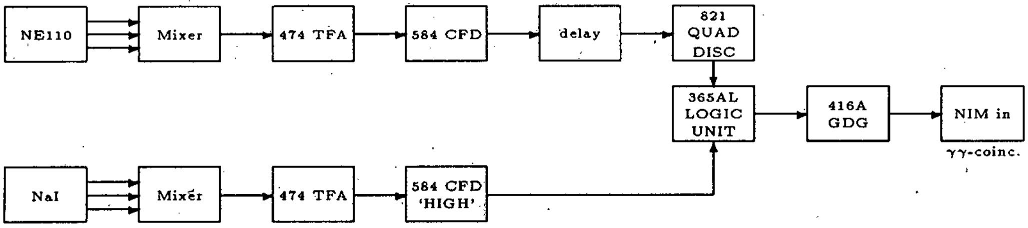

Figure 2.9: The plastic veto shield.

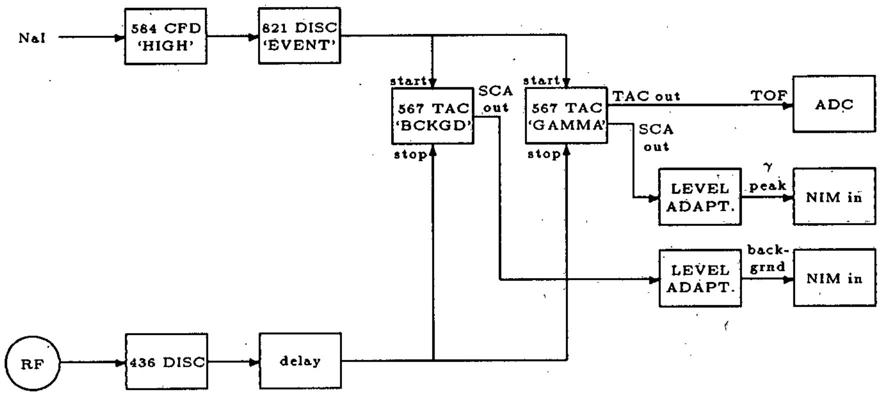

Figure 2.10: Neutron rejection by time-of-flight.

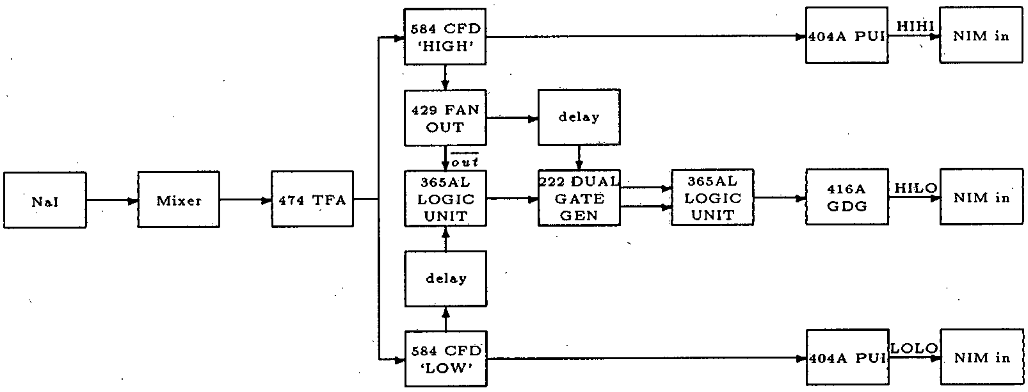

Figure 2.11: Pileup rejection.

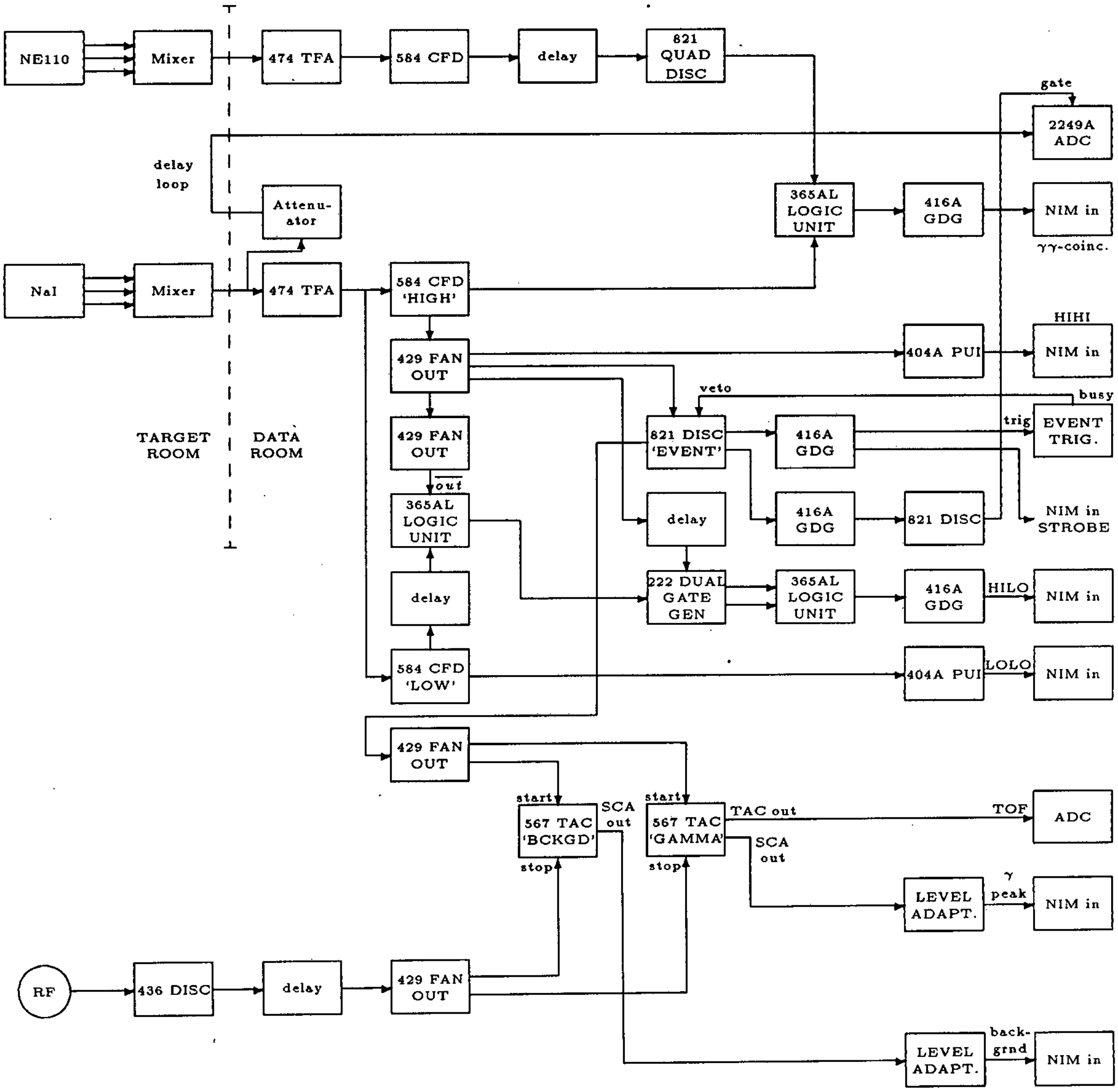

Figure 2.6: Electronics for the spectrometer HAGAR

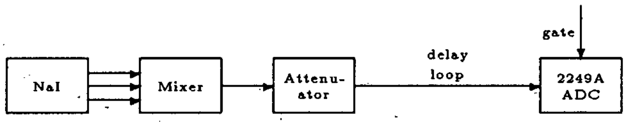

Figure 2.7: The NaI pulse handling.

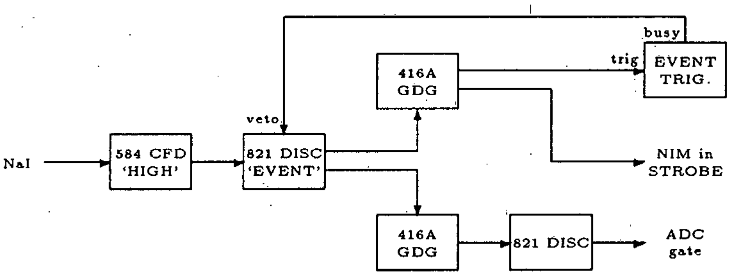

Figure 2.8: The event trigger.

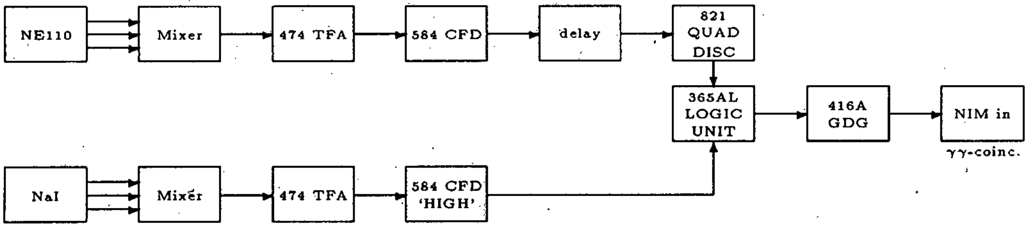

Figure 2.9: The plastic veto shield.

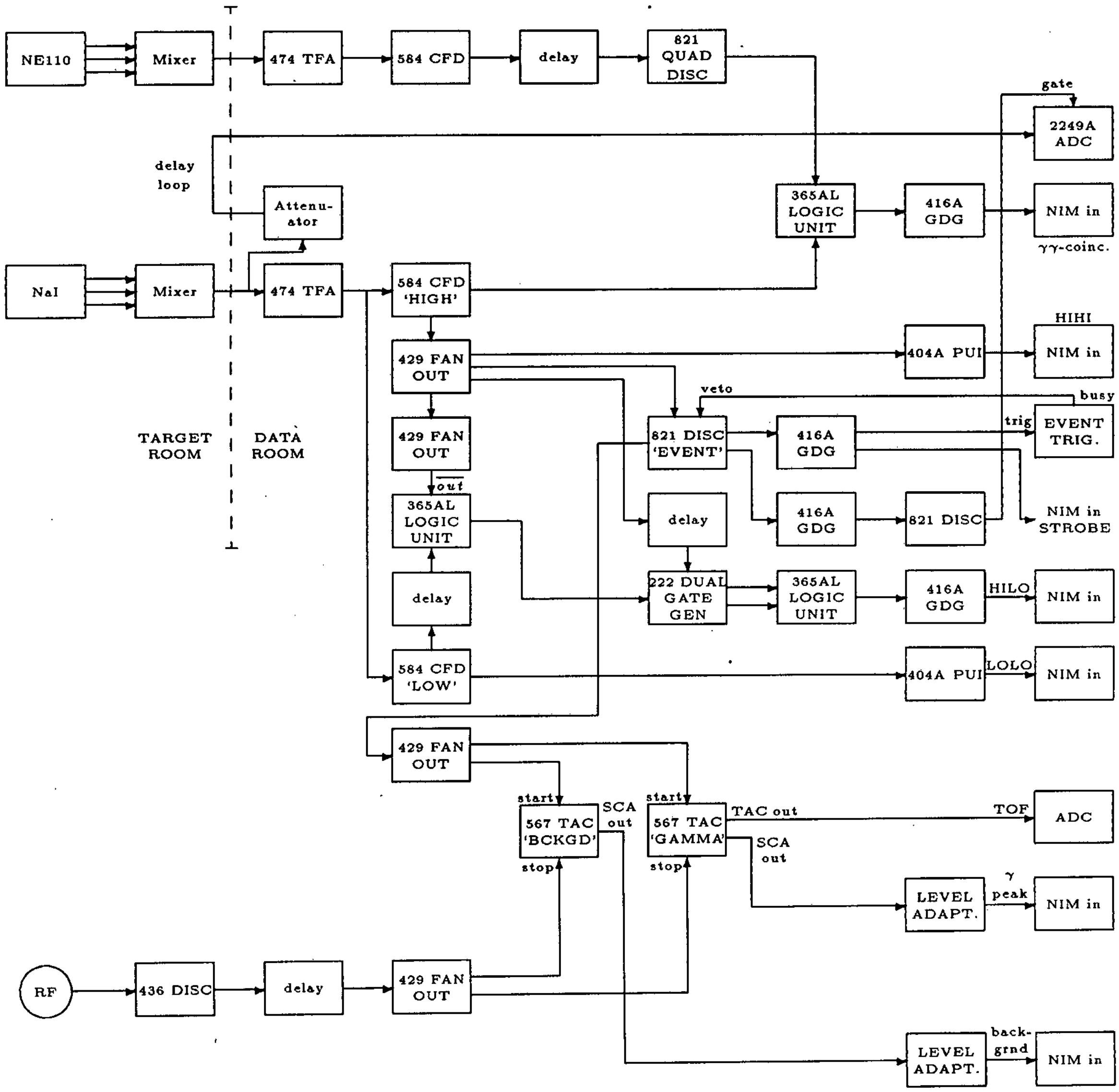

Figure 2.6: Electronics for the spectrometer HAGAR

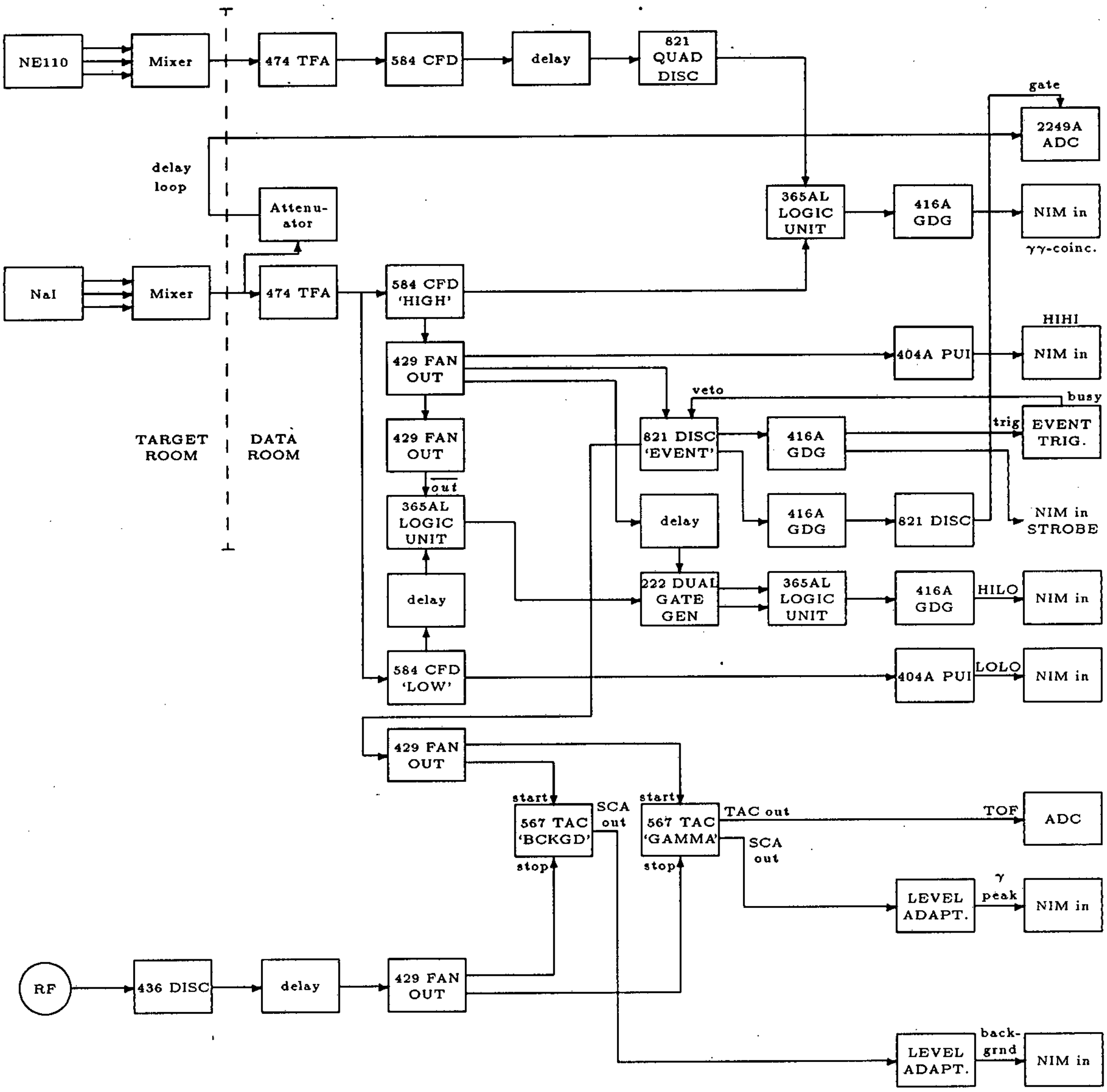

Figure 2.6: Electronics for the spectrometer HAGAR

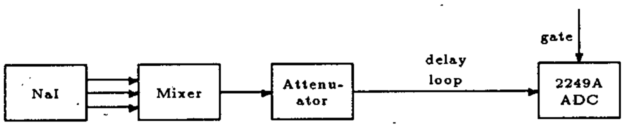

Figure 2.7: The NaI pulse handling.

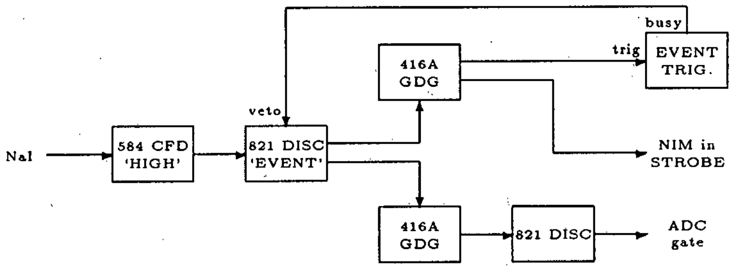

Figure 2.8: The event trigger.

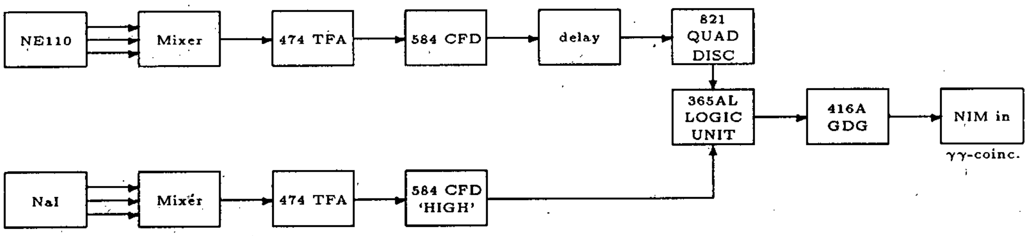

Figure 2.9: The plastic veto shield.

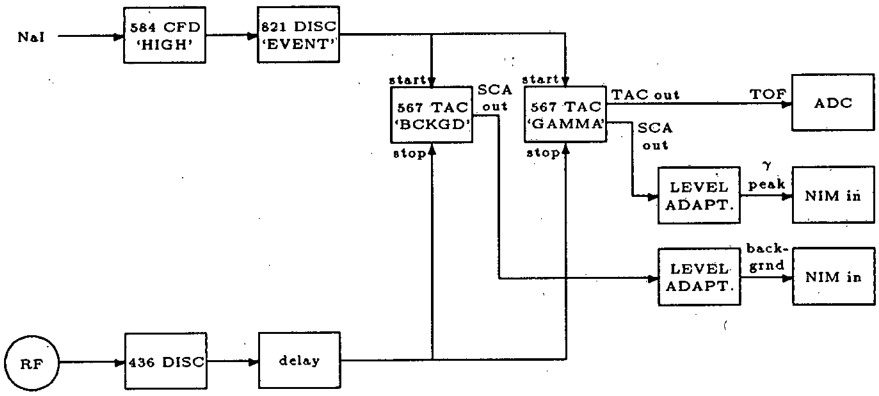

Figure 2.10: Neutron rejection by time-of-flight.

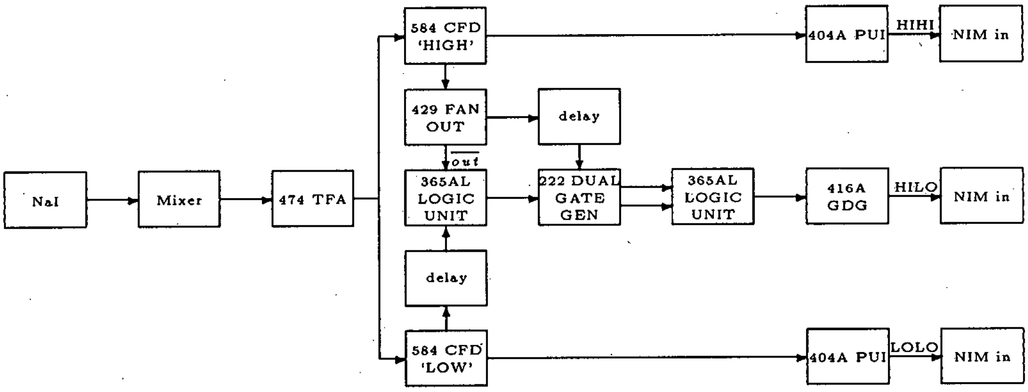

Figure 2.11: Pileup rejection.

Chapter 3

The Response Function of the Detector

3.1 The Monte Carlo Code

The signals of intermediate to high energy γ-rays in large NaI scintillators tend to have large low energy tails due to energy escape from the NaI crystal. It is also usual to find many states in this energy range that are very closely spaced and it is, therefore, very difficult, if not impossible, to determine the peak shapes and the background contribution from the γ-ray spectra alone. Good energy resolution in the spectrometer and the successful deconvolution of the spectra are thus critically dependent on good electronic rejection of background and escape events and an accurate determination of the detector response function. However, the stricter the rejection criteria, the lower the detector efficiency becomes, and some optimum balance must be found between the two. A Monte Carlo code [Zucc 86,Corv 81,Taiu 83] was used in the detector's design stage resulting in the final choice of detector dimensions given in Table 2.1. The evaluation of the detector response function is made difficult by the unavailability of very monochromatic photon beams above 10 MeV, and so the Monte Carlo code was used extensively for this purpose as well.

The program treats the detector as a set of up to eight coaxial, cylindrical elements, including a photon source, a main detector crystal, and up to two anticoincidence detectors and four shielding elements. When using this program, slight approximations had to be made in the dimensions of the lead collimator and the borax shielding to make them appear cylindrical for the calculations.

Energetic photons entering a NaI crystal may undergo Compton, photoelectric, or pair production reactions. Above a few MeV the dominant interaction process of photons in NaI is pair production, resulting in the creation of electrons and positrons. If the incoming photons are above ~20 MeV in energy, the energy losses of the conversion electrons due to bremsstrahlung becomes comparable or greater than ionization energy losses. The secondary photons generated will again be subject to the three processes mention above. In this way an electromagnetic shower will develop in the crystal. The program is thus set up to handle pair production, Compton, and photoelectric effects of photons, and the ionization, and bremsstrahlung energy losses of charged particles. If the energy of a secondary product falls below 30 keV it is assumed to be absorbed by whichever detector element it is currently in. Each primary photon and secondary particle is followed through the shower until it is absorbed. If the energy deposited in the anticoincidence shield is larger than some threshold (which is a parameter of the simulation), the event is rejected from the accepted response function. At the end of the simulation the program produces an array of 120 channels describing the shape of the response function with energy for a monochromatic incident photon beam. The array is scaled from zero energy at channel zero to the incoming photon energy at channel 100. This response function shape is due only to the energy absorption and conversion processes inside the detector.

One further step is necessary to produce a response function that can be used to deconvolute the experimental spectra, and that is to fold in a Gaussian shape to account for the statistical broadening of the signal in the photomultiplier tube. This arises from the fact that a discrete number of electrons is collected in the photomultiplier tube and will vary from event to event even though the energy deposited in the detector may be exactly the same. The width of this Gaussian is determined by comparing the simulated response function with the experimental spectra.

3.2 Determination of the Anticoincidence Threshold and Spreading Width

The raw gamma spectrum contains all the gammas seen by the NaI crystal, including those which are to be vetoed by the anticoincidence shield. This spectrum is thus independent of the threshold setting of the anticoincidence shield. An initial fit was, therefore, done to the three states of lowest excitation energy in the raw spectrum, in which the statistical spreading width was a parameter of the fit. (The energy calibration was also a parameter of this fit). Once we had determined the statistical spreading width for the response functions, we did a fit of the same states simultaneously to the accepted and rejected gamma spectra in which the anticoincidence threshold was a parameter. The rejected spectrum just mentioned is simply the difference between the total, raw gamma spectrum and the spectrum of accepted, 'good' gammas. Thus it contains any gamma that was thrown out because of pileup or, more importantly, by the anticoincidence shield logic. Since the threshold value determines the proportion of gammas that are assigned to the two spectra, these two spectra together contain more information about the threshold value than either one spectrum alone. In this fit the response functions for corresponding peaks were forced to vary by the same amount. The spreading widths and anticoincidence thresholds thus established were used for all later analysis. Most of these threshold values were consistent with what we believed the threshold to be, although in several cases the best fit was obtained for threshold values larger than we believe could have been the case. In cases where the energy resolution suffered due to some effect other than a high anticoincidence shield, for example pileup of pulses due to high beam current, it is to be expected that the fit will make the threshold value large to compensate for it. A test of the response functions produced in this way was done by fitting a set of peaks to a spectrum taken from a boron target. The spectrum is characterised by the well separated ground state and first excited state of carbon and other higher states, and the peak shapes are, therefore, more clearly evident than in the nitrogen spectra. Figure 3.1 shows how well the response functions duplicate the peak shapes in the energy region of interest.

3.3 Uncertainty in the Response Function Shape

Examination of many of the fits to the gamma spectra (see for example Figure 3.2) reveals a discrepancy between the data and the fit in the low energy shoulder of the γ_{2+3} peak. The literature indicates no state in this energy region, a region which is well studied. It therefore seems probable that this is due to some deficiency in the Monte Carlo code's prediction of the shape of the response function. Although a similar feature is not observed for any of the other states, it is likely that such a deficiency would be present in

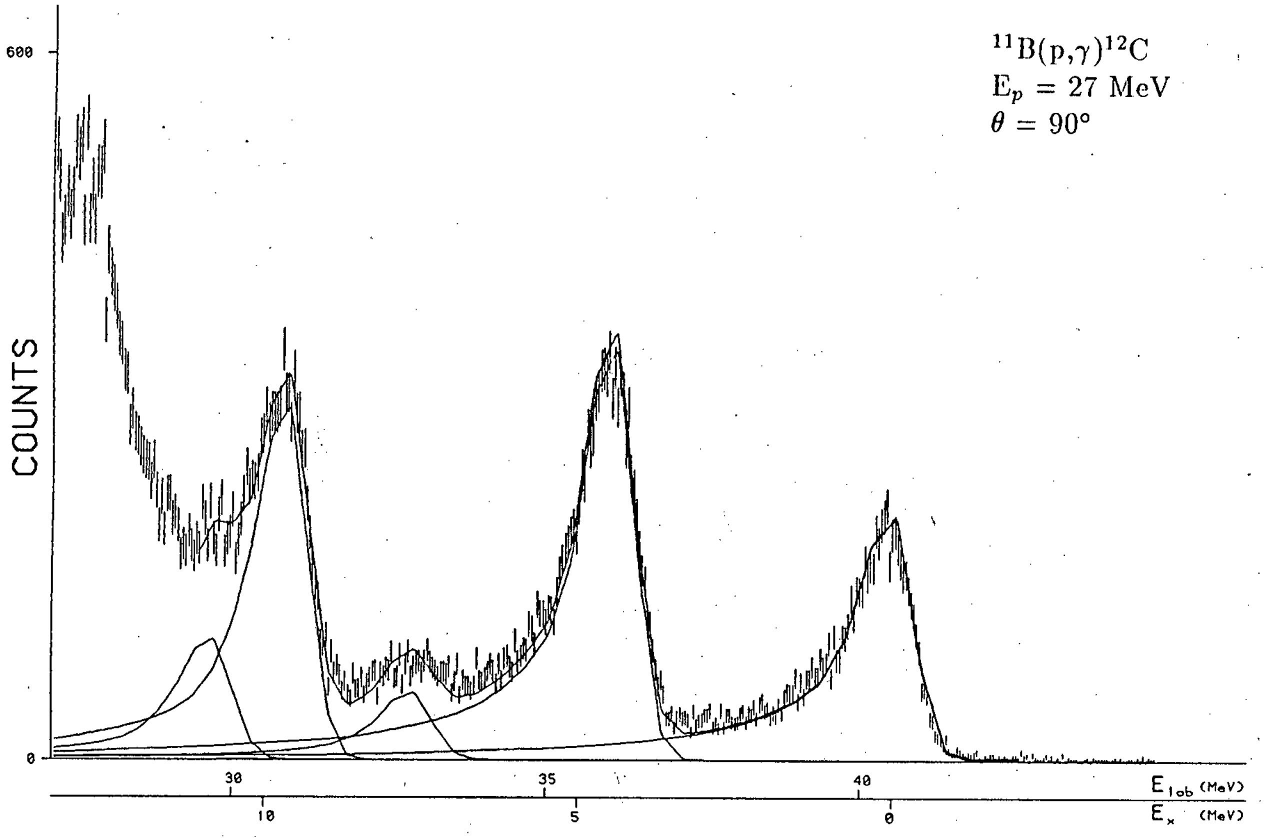

Figure 3.1: A fit to a spectrum from the ^{11}B(p,γ)^{12}C reaction showing how well the peak shapes are modelled.

the response functions for all energies and that it is not evident in the other peaks because their amplitudes are much smaller. In this case the shape deficiency would contribute to a systematic error in the determination of the strength of each transition. We are confident that no other deficiency in shape exists which could be larger than this, so this should provide an upper limit to the systematic error of our extracted differential cross-sections. In order to estimate this uncertainty the response functions produced by the Monte Carlo code were altered by the addition of a small Gaussian peak on the low energy shoulder. A new fit was made (see for example Figure 3.3) to several spectra, and the difference in the differential cross-sections obtained gave the uncertainty. As expected, only a small change was observed in the differential cross-section for the strong transitions to the γ_0 and γ_{2+3} peaks (less than 5%), while a change of up to 15% was observed for the weaker γ_1 peak. The next few excited states, which depend strongly on the size of the low energy tail of the γ_{2+3} peak, were observed to change by up to as much as 80% with the altered response functions. It is thus very obvious that we have to be much more confident in our understanding of the response function shape, as well as the background in the low energy region of the gamma spectrum before we can extend the analysis to the higher states. For this reason the current work is restricted to the analysis of the three lowest states.

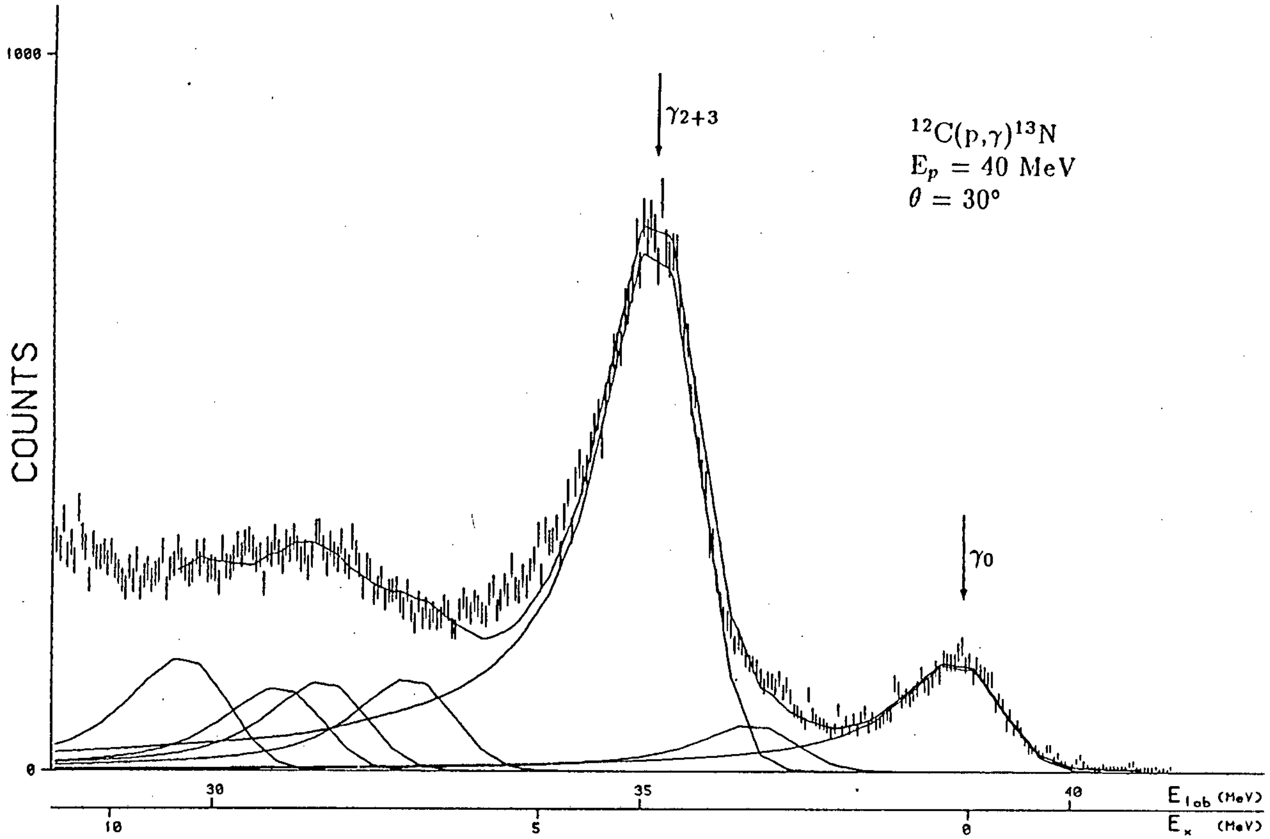

Figure 3.2: A fit to a typical gamma spectrum showing the inadequacy in the low energy shoulder of the γ_{2+3} peak.

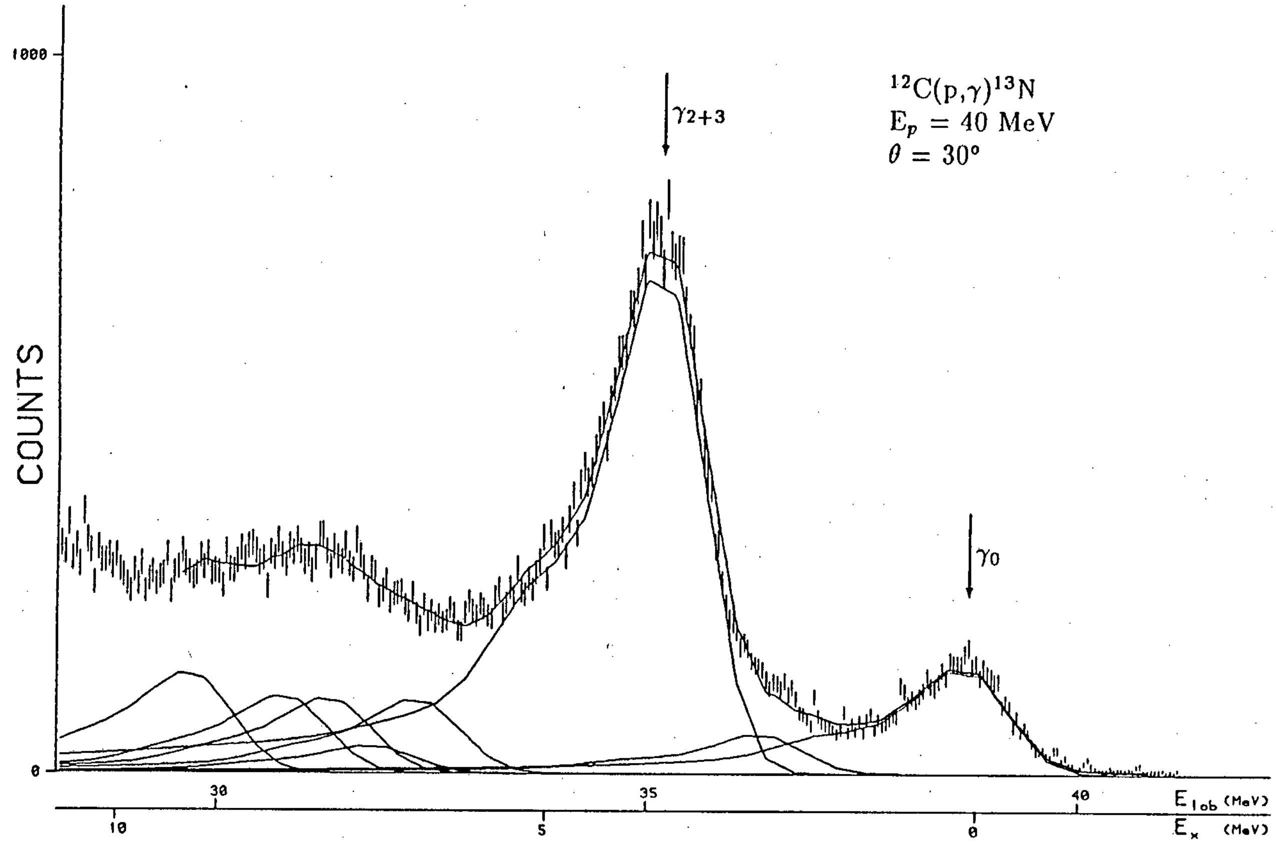

Figure 3.3: The improved fit to the same spectrum as in figure 3.2 using the altered response functions.

Chapter 4

Data Analysis

Once the response functions had been determined for different incoming photon energies and anticoincidence threshold settings, they were used to deconvolute the gamma spectra and extract the angular distributions. As mentioned in Section 3.2, the spectra were calibrated at the same time as the statistical spreading width was determined. The calibration was fixed by the positions of two prominent peaks. One is the peak due to the decay to the ground state of ^{12}C after excitation through the inelastic scattering channel ^{12}C(p,p$'$)^{12}C*(15.11). The amplitude of this peak is a few orders of magnitude larger than the peaks due to radiative proton capture. The other calibration peak is that due to the transition to the ground state of ^{13}N. The kinematics of the ^{12}C(p,γ)^{13}N reaction give the energy of this transition as

$$E_\gamma = \frac{T_P(M_R - M_P) + Q(T_P + M_R) + Q^2/2}{T_P + Q + M_R - \sqrt{T_P(T_P + 2M_P)}\cos\theta} - E_x \qquad (4.1)$$

where E_γ is the energy of the photon, T_P and M_P are the kinetic energy and mass of the projectile, M_R is the mass of the recoil nucleus, Q is the Q-value of the reaction, θ is the detector angle, and E_x is the final state excitation energy. A cosmic background is estimated by fitting a constant background to a region above the γ_0 peak. This is subtracted from the entire spectrum which is then unfolded by fitting to it a set of response functions at positions specified by the energies of the excited states of ^{13}N. Since the peak resolution has already been determined and the position is fixed, this leaves only the peak amplitude as a parameter of the fit. Although the current analysis is restricted to the three lowest states, eight peaks were included in the fits since there is considerable overlap between the low energy tail of the γ_{2+3} peak and the next few higher states. Omission of these higher states from the fits would lead to an overestimation of the strength of the γ_{2+3} peak as the fits tried to compensate for the absence of the higher states. We were able to get good fits to the data at low excitation energy by just fitting a set of response functions without a background contribution. This reflects the care with which the electronic discrimination circuitry was set up. Further justification for not including a background contribution in our fits was obtained [Fearick] from a simulation using the computer program CASCADE [Pühl 77] which predicted the statistical gamma-ray emission to be negligible in our region of interest. This procedure represents a change from that employed by other people. In particular Zucchiatti [Zucc 88], who did an independent analysis of the same data as used in this work, used a procedure of splitting the spectra into sections and then fitting a few peaks and a linear background in each section. These linear backgrounds are forced to match at the section boundaries and to be non-zero only from the particle decay threshold energy. This effectively means that his background only becomes significant for the γ_{2+3} peak and higher states. As expected this leads to good agreement for the strength of the γ_0 and γ_1 transitions between this work and that of Zucchiatti, but a difference in the strength of the γ_{2+3} transition. On the other hand, some other workers such as Hausman *et al.* [Haus 88] use empirically determined response functions which have a low energy tail that tends towards a constant (non-zero) value at low energies. In their fits to their gamma spectra they make do without a background in any energy region. The constant low energy tails, however, add up as a sort of step function which effectively replaces a background, including it in the strengths of the peaks. Unsurprisingly, they report larger strengths than are obtained in this work.

Our fits were done using the non-linear least squares minimization program MINUIT [Jame 75] from the CERN library. Response functions were generated for various energies with the Monte Carlo code in 5 MeV steps. These are read in by the fitting program and a peak shape is generated for the exact peak energy by a linear interpolation between the two closest response functions. The area of the fitted response function, N_γ, is used to calculate the differential cross-section for each transition by the relation

$$\frac{d\sigma}{d\Omega} = \frac{N_\gamma e_0 A}{Q \Delta\Omega \tau N_A \epsilon_c} \tag{4.2}$$

where e_0 is the unit charge, A is the atomic weight of the target nucleus, Q is the accumulated charge, $\Delta\Omega$ is the solid angle subtended by the detector, τ is the target thickness, N_A is Avogadro's number, and ϵ_c is the collection efficiency. For example, the number of photons in the ground state transition peak at $E_p = 48\,\mathrm{MeV}$ and $\theta = 75°$ (see figure 2.4) found by the best fit to the spectrum is $N_\gamma = 6309$. For this run the accumulated charge was $435.712\,\mu\mathrm{C}$ and the target surface density was $44.83\,\mathrm{mg/cm}^2$. The Monte Carlo program calculated that the detector efficiency was 15.5%, and since the detector subtends a solid angle of 19.2 msr, the differential cross-section is calculated to be 346 nb/sr. The statistical uncertainties on the differential cross-sections are obtained from the contributing uncertainties by adding them in quadrature. Of these contributions the largest is the uncertainty on the number of photons in each peak. The uncertainty in the efficiency is the next largest and is usually a factor of 5 to 10 smaller than the uncertainty of N_γ.

For comparison of the angular distributions with theory, the angles of observation and observed differential cross-sections must be transformed to the centre-of-momentum reference frame. This is done by the kinematic relations

$$\tan\theta_{CM} = \frac{\sin\theta_{Lab}}{\Gamma(\cos\theta_{Lab} - B)} \tag{4.3}$$

and

$$\left[\frac{d\sigma}{d\Omega}\right]_{CM} = \frac{\sin^3\theta_{Lab}}{\Gamma\sin^3\theta_{CM}(1 - B\cos\theta_{Lab})}\left[\frac{d\sigma}{d\Omega}\right]_{Lab} \tag{4.4}$$

where B is velocity of the centre-of-momentum frame relative to the laboratory frame and $\Gamma = (1 - B^2)^{-1/2}$. The centre-of-momentum angular distributions are then fitted with a sum of Legendre polynomials [Gian 85] of the following form:

$$\frac{d\sigma}{d\Omega} = \sum_{i=0}^{4} A_i P_i(\cos\theta) \tag{4.5}$$

The summation is taken up to P_4 to include quadrupole components. Terms higher than P_4 would indicate the presence of higher multipolarity radiation which is not expected and should in any case be two factors of kR smaller [Gian 85] in magnitude if present ($R \sim$ the dimension of the nucleus). The total cross-section is then given by integrating Eq. (4.5) to get

$$\sigma = 4\pi A_0 \tag{4.6}$$

Due to the size of the detector, measurements could only be made at angles from approximately 30° to 150° to the beam direction, and additional constraints had to be imposed on the fits to prevent them from becoming negative or curving upwards at extreme angles. Although the sum of Legendre polynomials is linear in the coefficients A_i, the additional constraints made the fit a non-linear one and the code MINUIT [Jame 75] was again used. The results of these fits are presented in figures 4.1 to 4.8. The error bars plotted in these figures are just the statistical uncertainties of the various components of equation 4.2 which have been added in quadrature. A crude calculation can show that these are reasonable as follows: examination of the γ_0 transition at $E_p = 40\,\mathrm{MeV}$ and $\theta = 30°$ (figure 2.4) reveals approximately 8000 counts in the peak (a significant contribution of which lies in the low energy tail). The uncertainty in this area will then be of the order of $\sqrt{8000}/8000 = 1.1\%$. This is the dominant contribution and is combined with the other contributions from equation 4.2 to get the overall uncertainty of ~1.7% which is the plotted error bar for this point. In this case, as is the case for many of the points in the γ_0 and γ_{2+3} curves, these error bars are virtually the same size as the plotting symbol and thus not clearly visible. As expected, they are generally larger for the γ_1 data. Note that these error bars do not include any systematic uncertainty. As mentioned previously, the systematic uncertainty is dominated by the uncertainty in the shape of the response function and can be as large as 5% (or 15% for the γ_1 points). These uncertainties would swamp the statistical uncertainties if plotted, and are thus omitted from the differential cross-section plots. It appears obvious from inspection of the differential cross-sections that this systematic uncertainty is grossly overestimated for many of the data (see for example the γ_0 data for $E_p = 40\,\mathrm{MeV}$), but may well be reasonable for other points (for example the data at $E_p = 50\,\mathrm{MeV}$). The angular distributions for each transition are presented again in figures 4.9 to 4.11, but this time superimposed on the same axes for easy comparison. It is clear that the total cross-section (which is the integrated area under the angular distribution curve) increases with beam energy up to $E_p \approx 46$ MeV, after which it decreases again. This resonant behaviour is shown more explicitly in figure 4.12 which plots the variation of total cross-section with beam energy. The data presented in this figure are calculated by equation 4.6. The values obtained from this formula have been checked by numerical integration of the angular distribution curves and are in excellent agreement with them. The error bars plotted in this figure are the systematic uncertainties due to the response function shape. The statistical uncertainties due to the fits to the angular distributions are very small compared with the systematic errors. Visual inspection of the fits confirms that for most of them the uncertainty in the integrated area is indeed small.

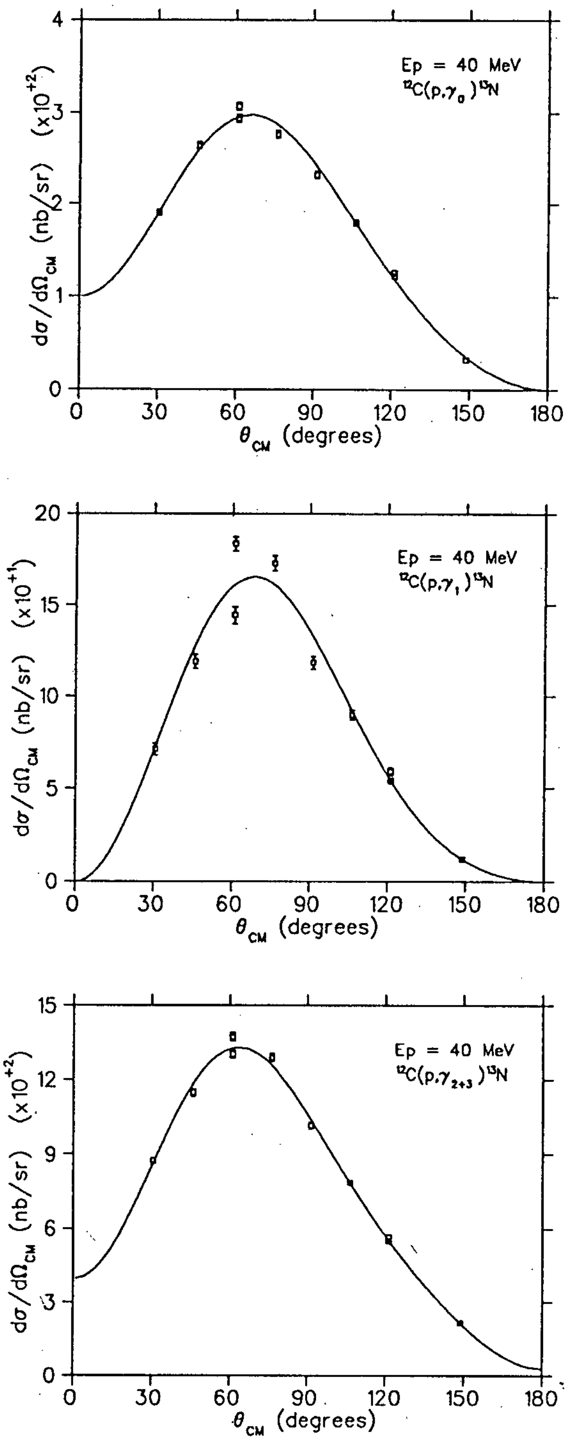

Figure 4.1: Gamma ray angular distributions observed at a beam energy of 40 MeV. The solid line represents a fit made using Eq. (4.5).

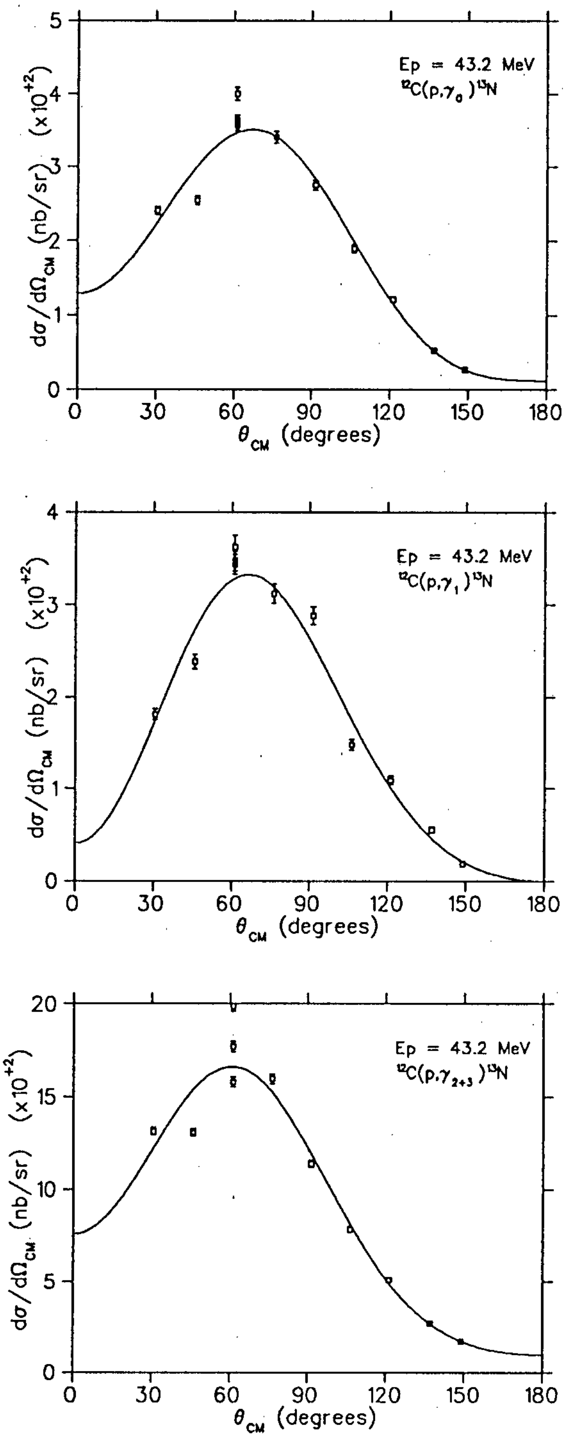

Figure 4.2: The same as figure 4.1 for a beam energy of 43.2 MeV.

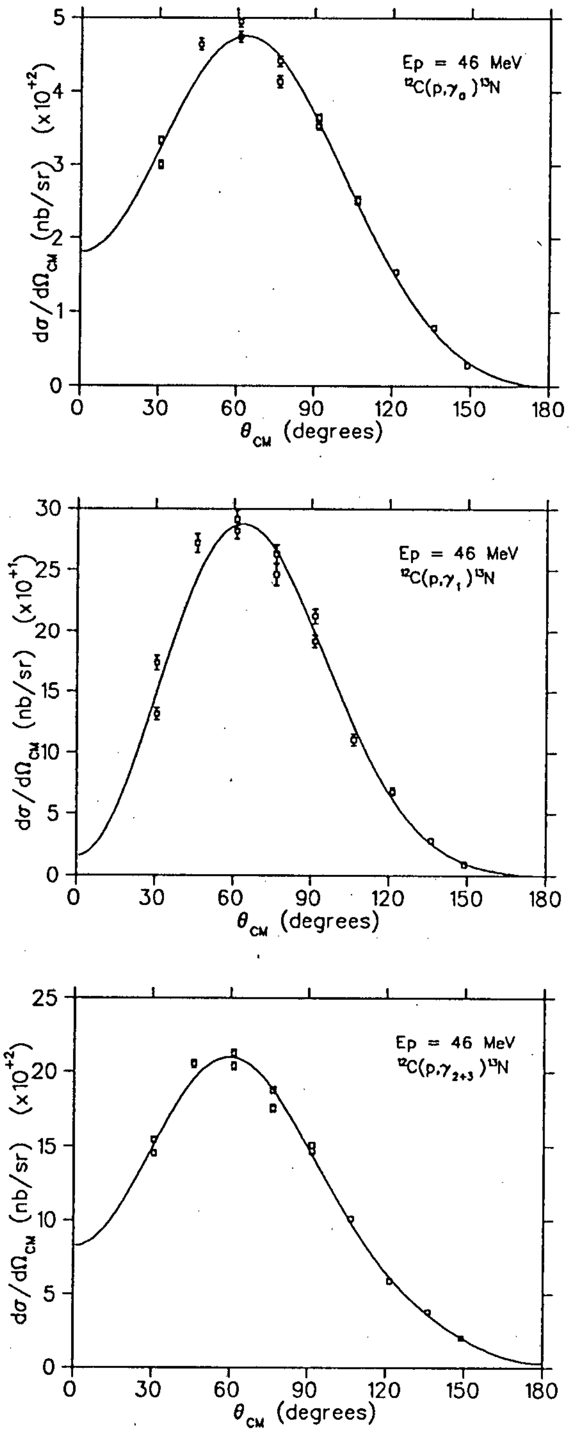

Figure 4.3: The same as figure 4.1 for a beam energy of 46 MeV.

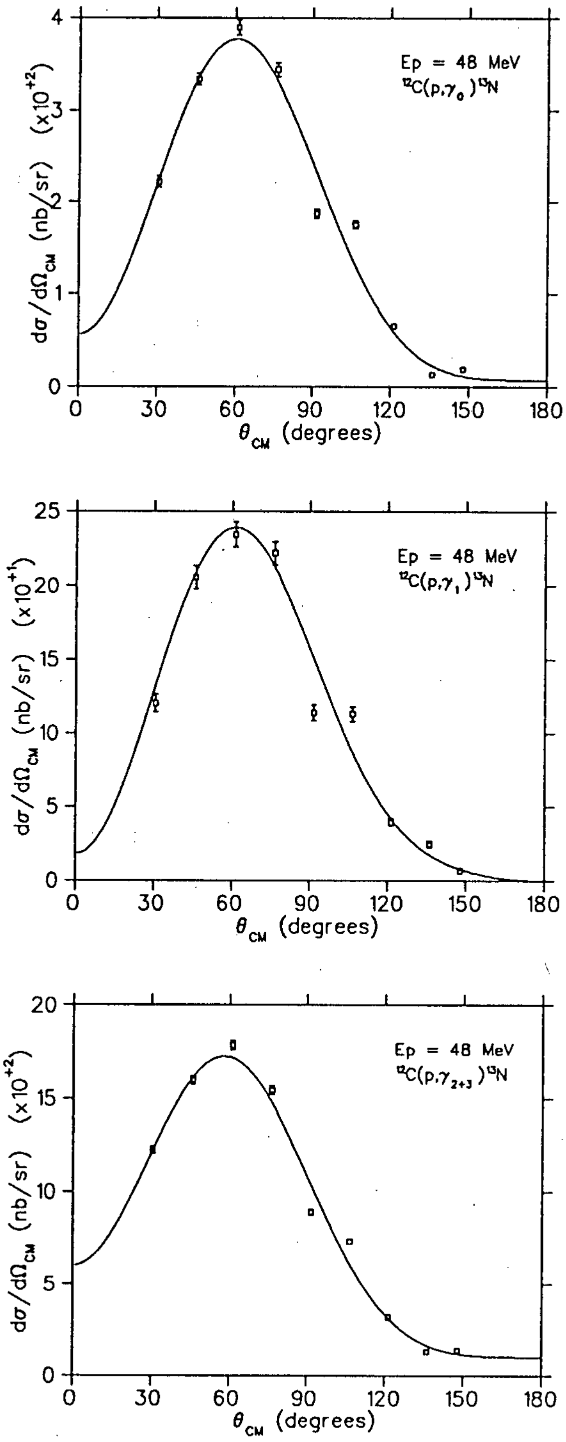

Figure 4.4: The same as figure 4.1 for a beam energy of 48 MeV.

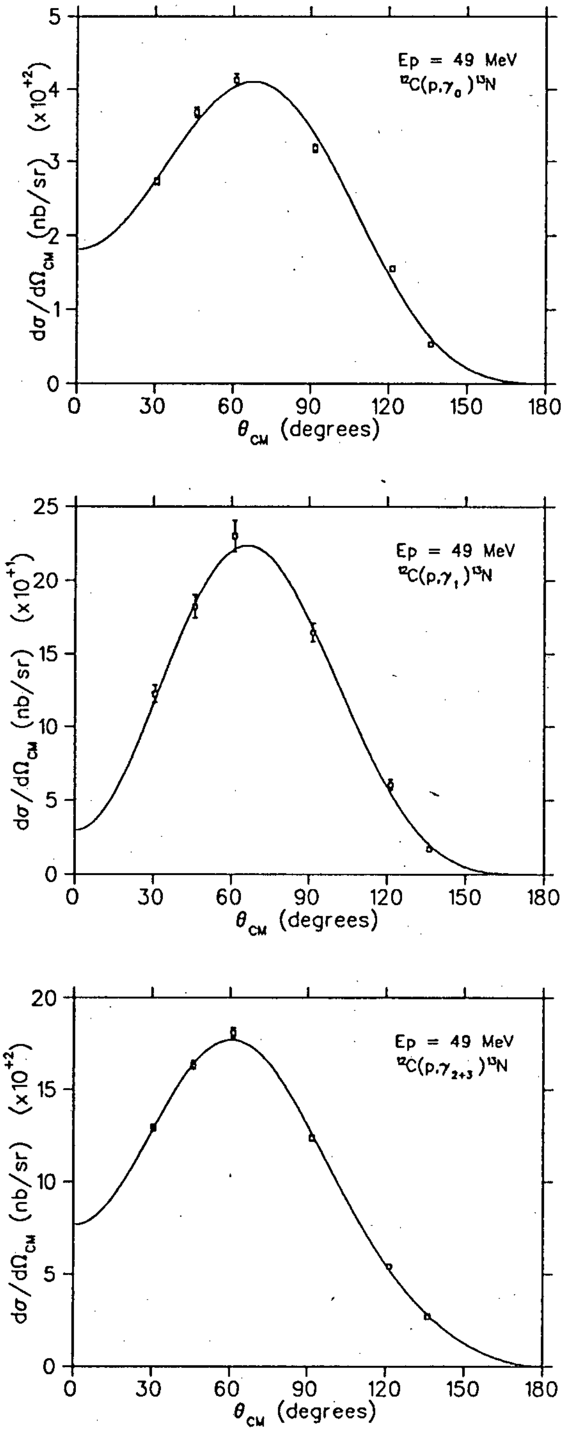

Figure 4.5: The same as figure 4.1 for a beam energy of 49 MeV.

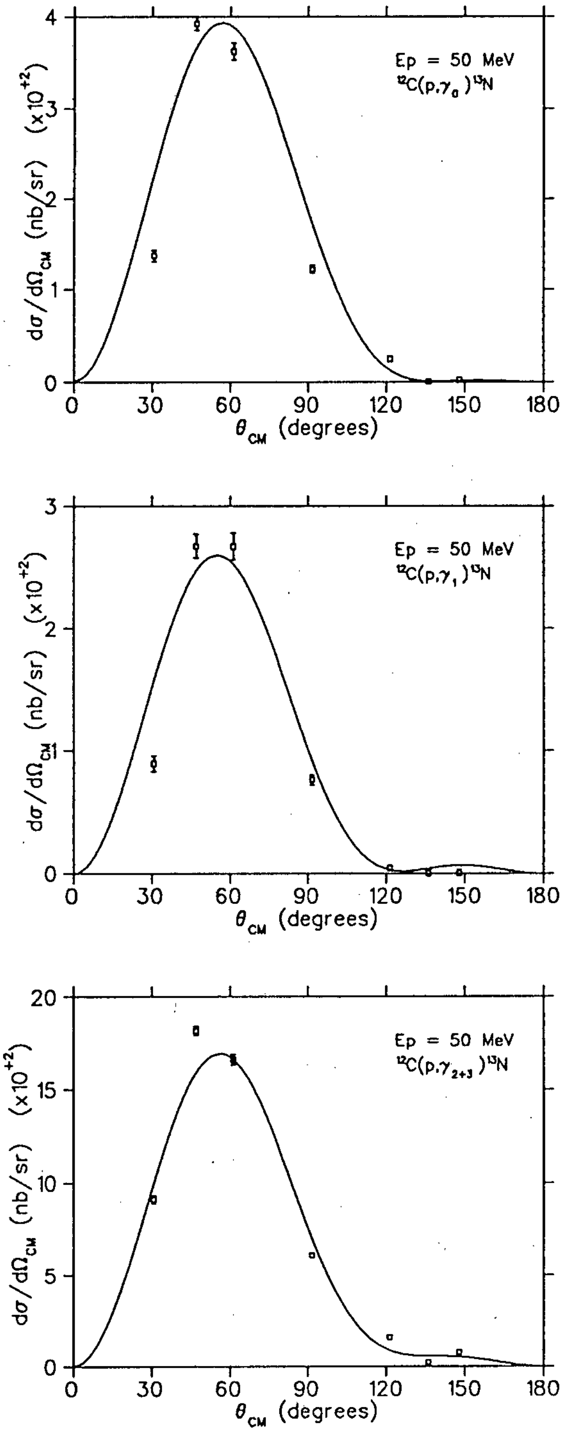

Figure 4.6: The same as figure 4.1 for a beam energy of 50 MeV.

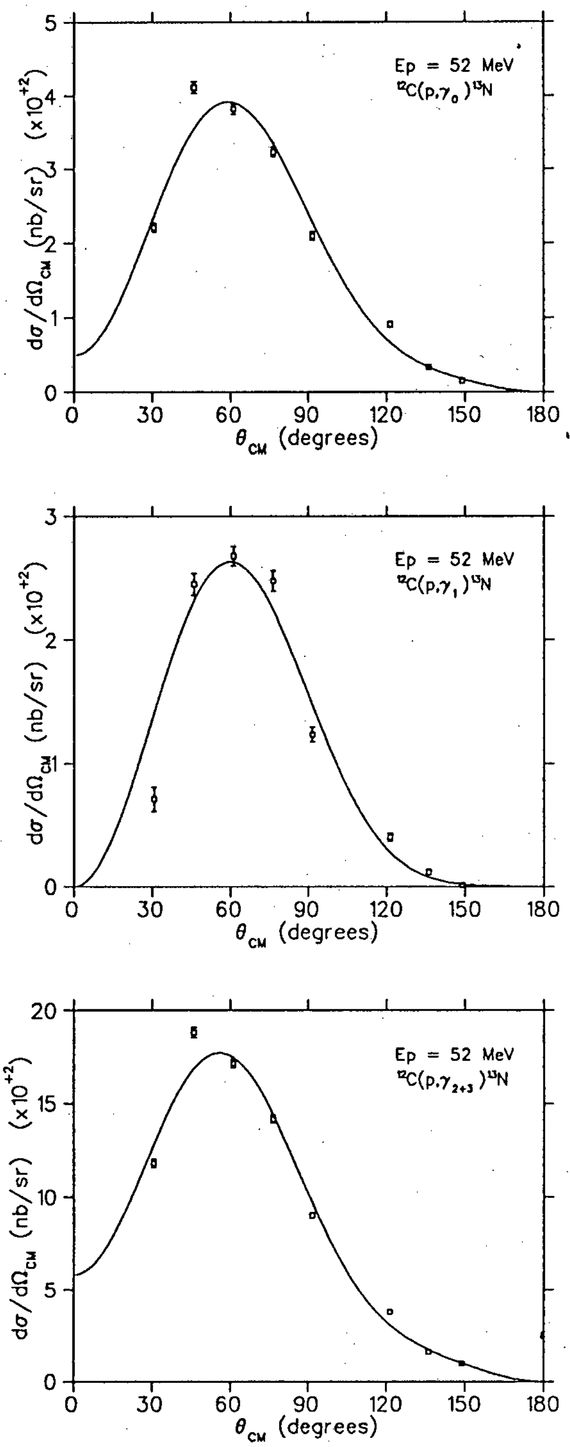

Figure 4.7: The same as figure 4.1 for a beam energy of 52 MeV.

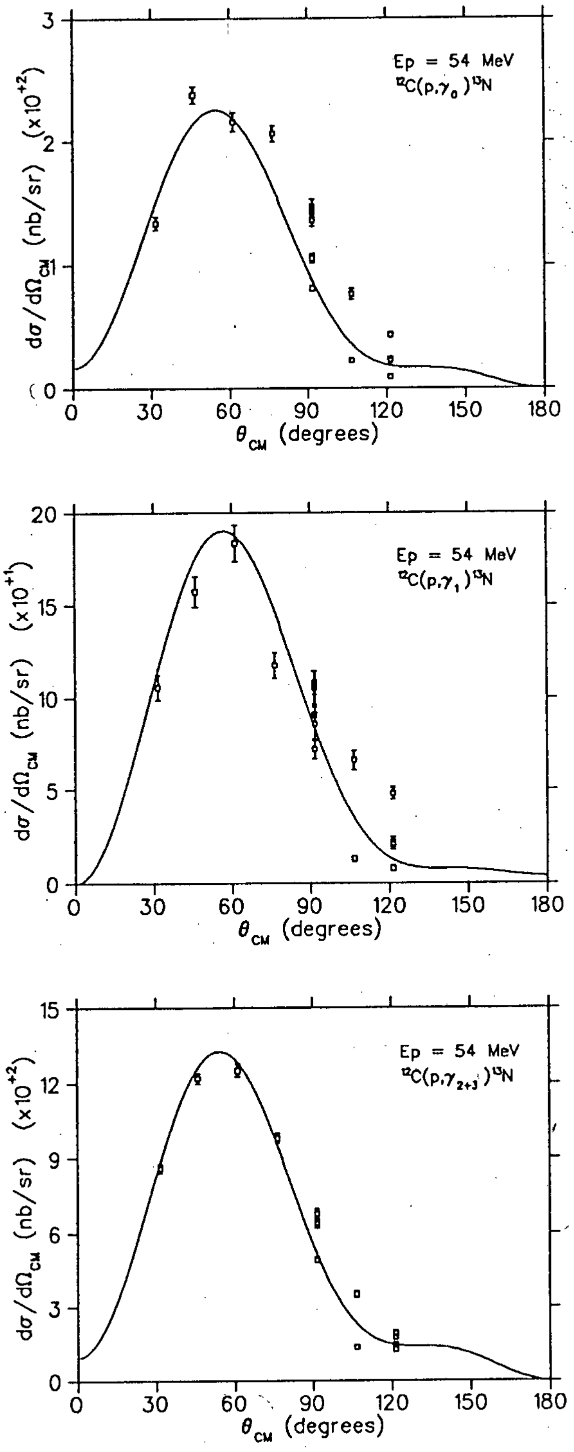

Figure 4.8: The same as figure 4.1 for a beam energy of 54 MeV.

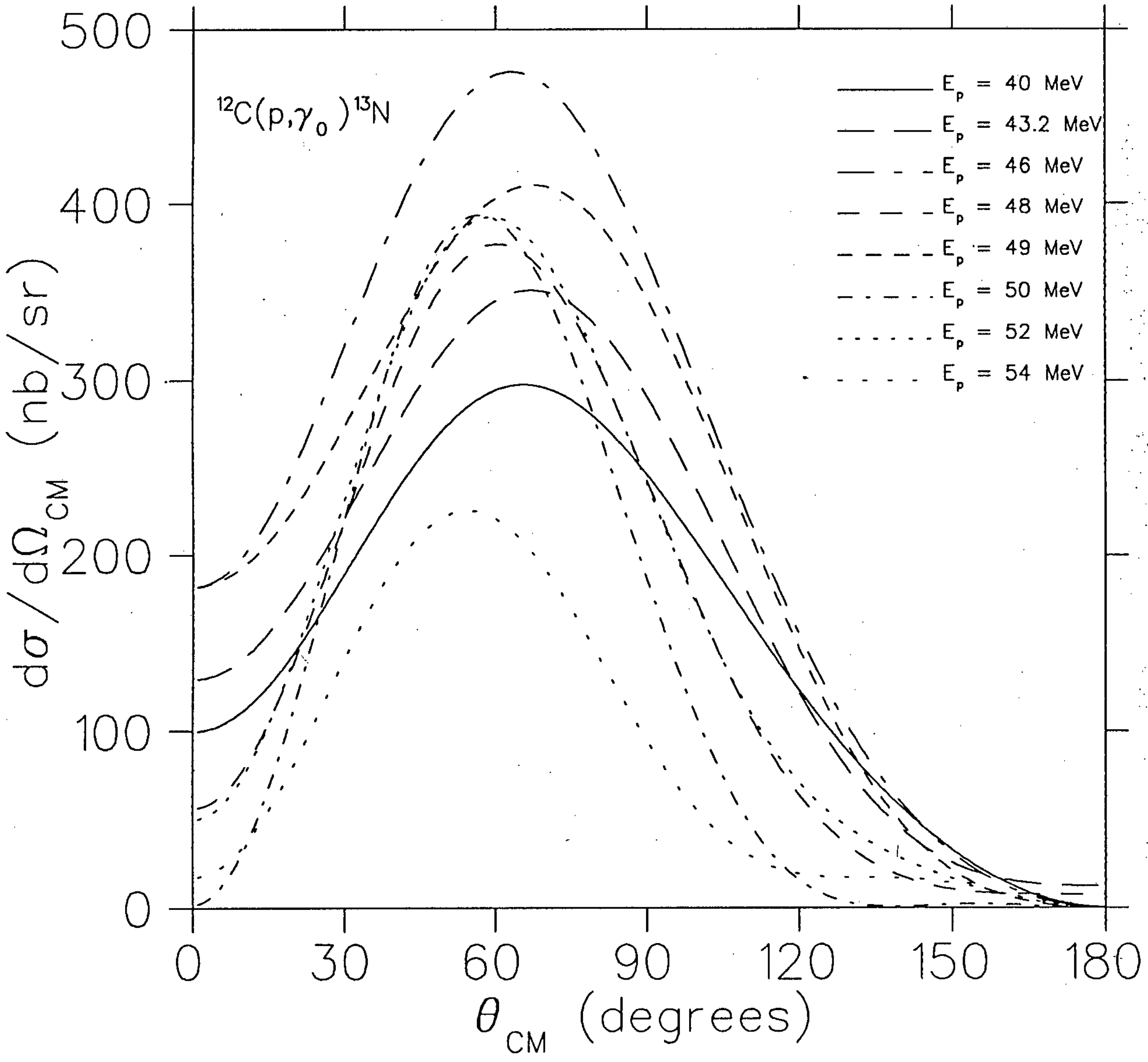

Figure 4.9: A comparison of angular distributions for the transition to the ground state of ^{13}N for all beam energies measured.

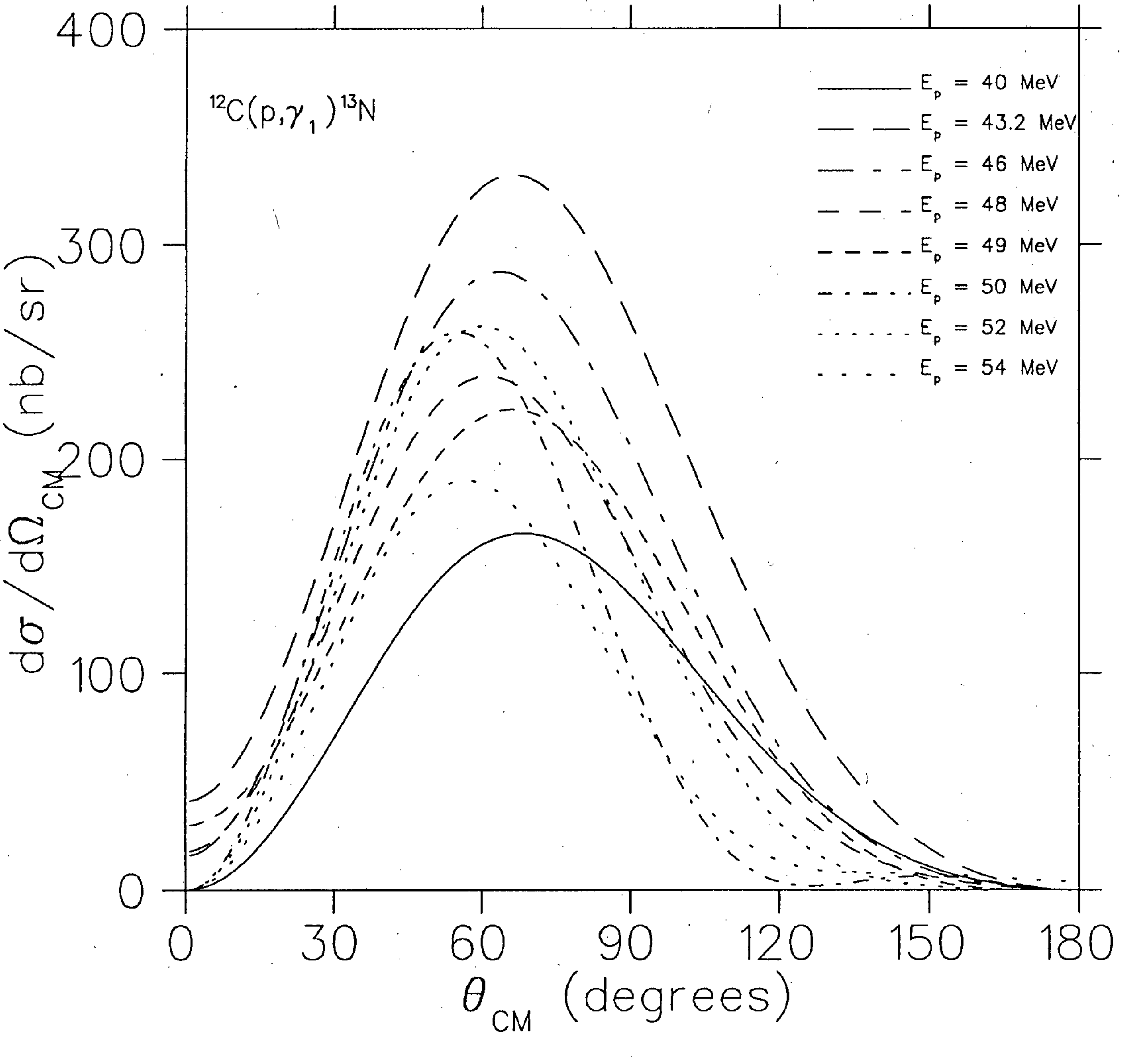

Figure 4.10: The same as figure 4.9 for the transition to the first excited state of ^{13}N.

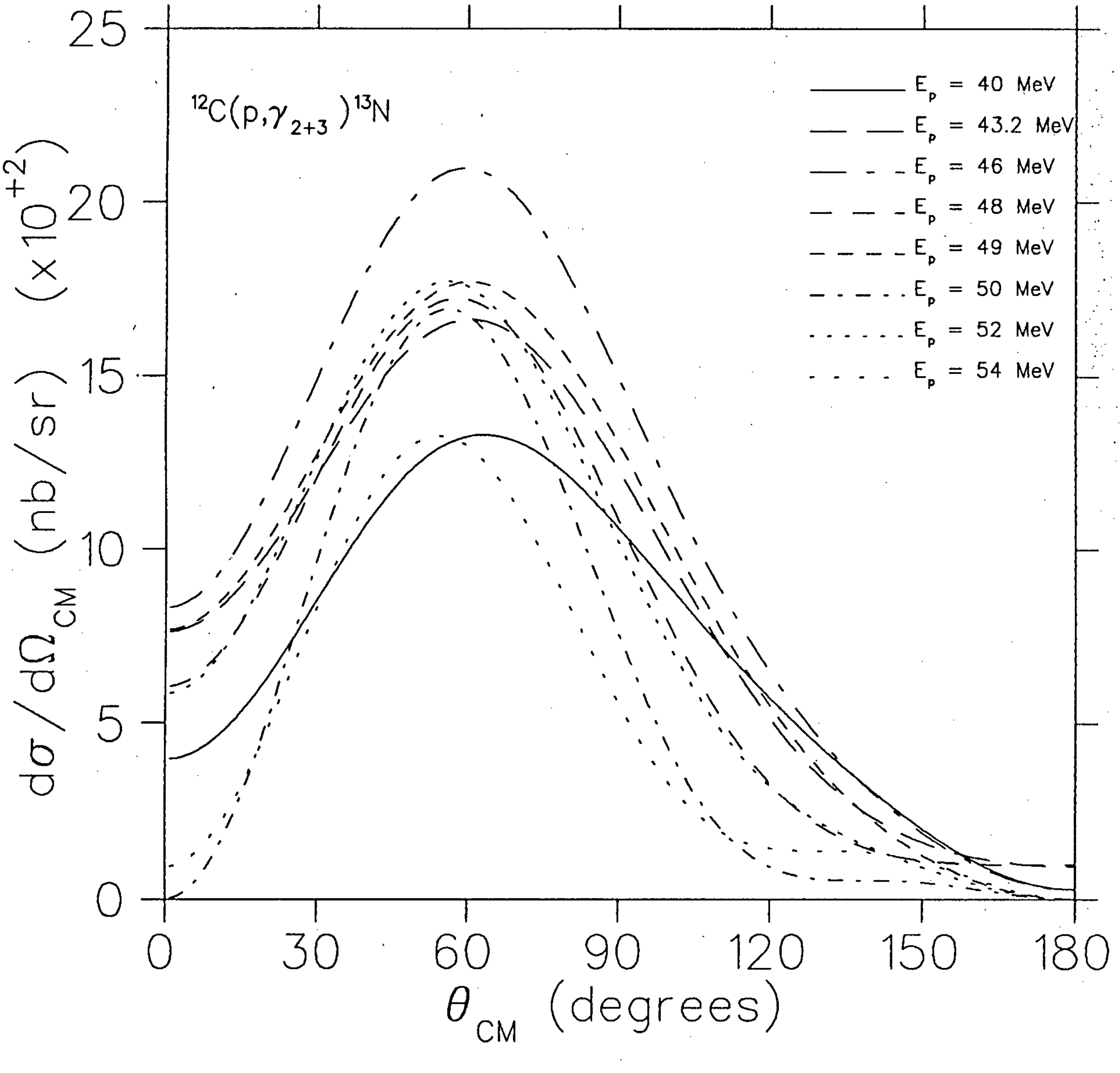

Figure 4.11: The same as figure 4.9 for the transition to the unresolved second and third excited state of ^{13}N.

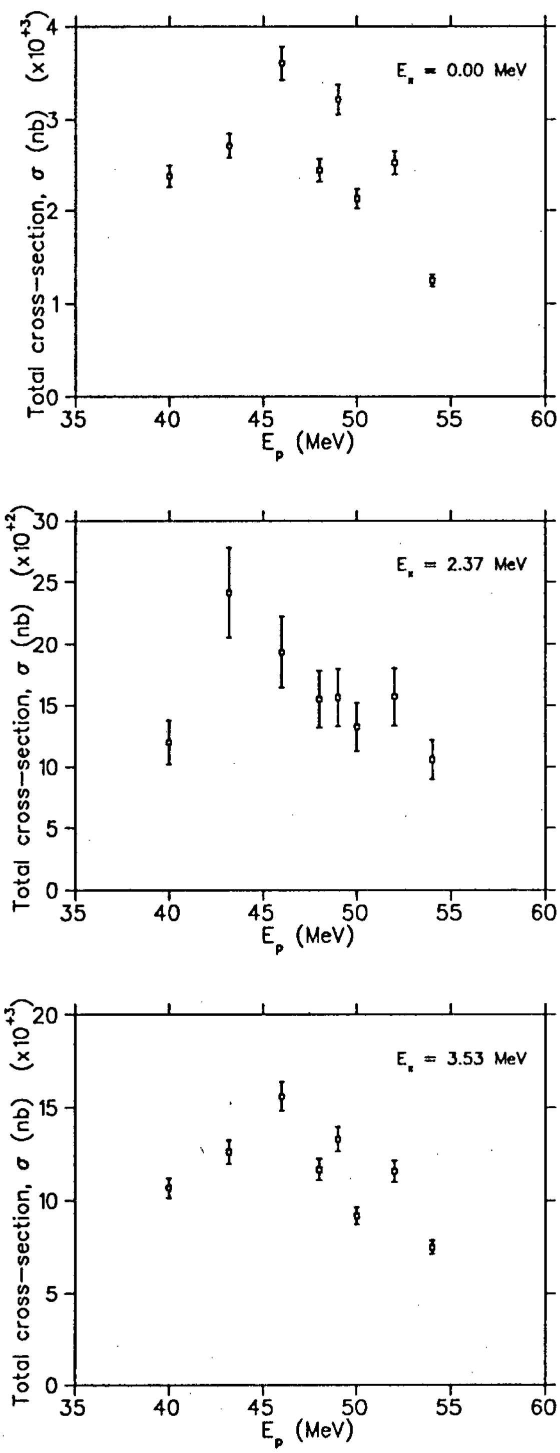

Figure 4.12: The variation of total cross-section with beam energy.

Chapter 5

Discussion

Inspection of the gamma spectra acquired during this experiment reveals many interesting features. On the low energy side of the spectra (see for example figures 5.1 to 5.3) are the gammas from inelastic scattering on ^{12}C. These are produced when the incident protons scatter inelastically off ^{12}C nuclei raising them into excited states which subsequently decay back down to the ground state with the emission of a photon. As expected, these reaction channels are orders of magnitude more likely than the radiative capture channels, and the inelastic scattering peaks go way off scale on the above-mentioned figures. In order not to have the radiative capture gammas, in which we have the greatest interest, swamped by inelastic scattering gammas, most of the latter are not counted by setting a low energy threshold on the data. This threshold was set just below the 15.11 MeV peak from the inelastic proton scatter off ^{12}C, which was included for energy calibration purposes as well as for possible normalisation of cross-sections.

On the high energy ends of the above-mentioned gamma spectra are the features due to radiative decays from excited states of ^{13}N populated by proton capture on ^{12}C. We observed proton beam energies from 40 MeV to 54 MeV which allows the population of states of ^{13}N around the second harmonic of the giant dipole resonance. The decay from these states directly down to the ground state is responsible for the gamma peak of highest energy. This, along with the transition to the unresolved second and third excited states at 3.51 MeV and 3.55 MeV, are the two transitions with the greatest strength. The transition to the first excited state of ^{13}N at 2.37 MeV is less strong and usually visible as a shoulder on the high energy side of the γ_{2+3} peak. The transitions to higher excited states of ^{13}N rapidly become unresolvable to the eye as level density increases and transition strength decreases.

A large, broad bump is visible in the two spectra of higher beam energy centred near channel 380 in figure 5.2 corresponding to an excitation energy of ~24.5 MeV, and channel 325 in figure 5.3 corresponding to ~25 MeV. The corresponding bump for figure 5.1 in which the beam energy is lower lies underneath the large inelastic scattering background. This is believed to be due to the transition from the second harmonic to the first harmonic of the giant dipole resonance. One last prominent feature is a sharp peak just below the broad bump (see for example figure 5.1 at about channel 390). This peak is present in most spectra, although its strength varies greatly. It is believed to be a pileup effect which our electronic rejection scheme failed to detect. The energy of these peaks corresponds almost exactly to the expected energy summed from a 15.11 MeV and a 4.44 MeV inelastic scatter on ^{12}C. There appears to be a fairly strong correlation between the strength of this peak and the proton beam current. The spectrum in figure 5.1, for instance, which has a prominent peak, was acquired with a high beam current of 50 nA, while the spectrum in figure 5.3 in which this feature is hardly visible was acquired with a beam current of just 10 nA. However, this effect is not simply dependent on beam current as figure 5.2 shows in which this peak is very small even though the beam current was 50 nA. At present this effect is not fully understood.

It is obvious from the above that to extract information with any degree of confidence from this region of the data, one has to understand the response of the detector and the background very well. Until such a situation is achieved, it is meaningless and misleading to push the analysis into this region. For this reason we have concentrated our efforts so far on the transitions to the ground state and the first two excited states of ^{13}N. Extensive effort has gone into using the Monte Carlo code to predict the shape of the detector's response function. The good fits we have achieved with these response functions on spectra from carbon and boron targets give us confidence in their accuracy. We also believe that the background under this high energy part of the spectra is very small or zero, partly because of the good fits we get without the inclusion of a background, and also because of the calculations done with the code CASCADE [Pühl 77]. From this basis we can begin to extend the analysis to higher states.

The angular distributions presented in figures 4.1 to 4.8 show the measured data and the best fits to that data of a series of Legendre polynomials. It is unfortunate that, due to the size of the detector, it was not possible to get closer than 30° to the beamline. The absence of differential cross-section data at extreme angles allows the best fit to the data to do unphysical things, such as becoming negative or arbitrarily large at extreme angles. Additional constraints had to be imposed during the fitting procedure to prevent this. It should be noted that we are effectively using the fitted function to interpolate the differential cross-section at the missing points. It is always desirable to interpolate as little as possible beyond the measured endpoints of a function since the trend of the function at the extremes can make a large difference to the integrated area under the curve which in this case is the total cross-section. In all of our angular distributions, the fitted curve tends to zero at large angles, but varies at low angles. The goodness of our fits, however, reinforce our belief that this variation is due to a variation of the relative intensities of the radiation multipoles and not to bad interpolation. The low differential cross-section in the forward direction and the peaking at about 60° to the beam direction in the lab frame indicate the predominance of low order multipole radiation. This has been attributed (eg. [Zucc 88,Ferr 76]) predominantly to E1 radiation with large E2 interference and possibly a small amount of M1 interference. The best comparison of the angular distributions is probably obtained by examination of figures 4.9 to 4.11 which show the fitted curves drawn on the same axes. The measured data in these pictures are left out in the interests of clarity. The resonant behaviour is immediately obvious, with the integrated cross-section (the area under each curve) increasing with beam energy up to $E_p \approx 46$ MeV and then decreasing again. A variation in peak position between 55° and 70° is also evident. The shape of the angular distributions appears not to vary much, with the exception of the 40 MeV curves which are broader than the others.

The total cross-sections (figure 4.12) show explicitly the evidence for resonant behaviour of the transitions to the low-lying states of ^{13}N. The cross-sections for the γ_{2+3} transition are nearly a factor of five larger than the cross-sections for the γ_0 transition at all measured energies, while the cross-sections for the γ_0 transition are about a factor of two larger than for the γ_1 cross-sections. The variation of cross-section with beam energy for the transitions to the ground state and unresolved second and third excited states show remarkable similarity. Both peak at about 46 MeV and both have a FWHM larger than 11 or 12 MeV. A beam energy of 46 MeV corresponds to an excitation of about 44 MeV in ^{13}N, and thus a maximum photon energy from a transition to the ground state of 44 MeV. This is then the centroid excitation energy of the second harmonic of the giant dipole resonance. If this is indeed just twice the excitation energy of the first harmonic, then that puts the centroid energy of the first harmonic at about 22 MeV. This is in fair agreement with other workers (for example [Berg 76,Ferr 76]) who show fragmentation of the first harmonic giant dipole resonance with a large part of the strength at 20.5 MeV for the γ_0 transition, just less than 22 MeV for the γ_1 transition and at about 26 MeV in the γ_{2+3} case. Our cross-section for the transition to the first excited state of ^{13}N is a little different to what we see for the other two transitions. It peaks at about 43 MeV, slightly lower than the other two. It is also a little narrower than the other two. It is possible that these differences are at least partially due to the fact that the gamma peak corresponding to this transition is not well resolved from the γ_{2+3} peak and is much smaller than that peak. Any uncertainty in extracting the areas of the two gamma peaks would affect the γ_1 data much more than the γ_{2+3}. The uncertainty in the total cross-section due to the possible variation of the fits to the angular distributions is small, as the figures show, and the overall uncertainty is thus dominated by the systematic uncertainty. As described in section 3.3 this is dominated by the uncertainty in the shape of the response functions produced by the Monte Carlo program. The error bars on the total cross-sections thus represent the systematic error due to the response function shape and are 5% for the γ_0 and γ_{2+3} cross-sections and 15% for the γ_1 cross-sections.

A comparison of our differential and total cross-sections with some other works confirms what we expected from the differences in gamma spectrum fitting procedures. In the case where the response function is empirically determined and is given a long, constant low energy tail the published values for the differential cross-sections are much larger than our values. The points at 90° of Fisher *et al.* [Fish 63] are about a factor of two larger than ours, and those of Blatt *et al.* [Blat 84] at 60° are nearly a factor of three larger. On the other hand, Zucchiatti's values for the differential and total cross-sections [Zucc 88] are about 25% lower than ours due to his inclusion of a background in his fits. One final note of concern is the fluctuation of total cross-section around 48 to 52 MeV. This is present in all three transitions and is larger than the quoted uncertainties, but is not believed to be real. At present we believe that it is due to high beam current and pileup effects which are not fully understood. It would, therefore, be advisable in future to repeat measurements in this region to remove this uncertainty. Such a step could very well result in much more compelling evidence for resonance. Therefore, at present we can only tentatively conclude that we have observed evidence for resonant behaviour in the transitions to the low-lying states.

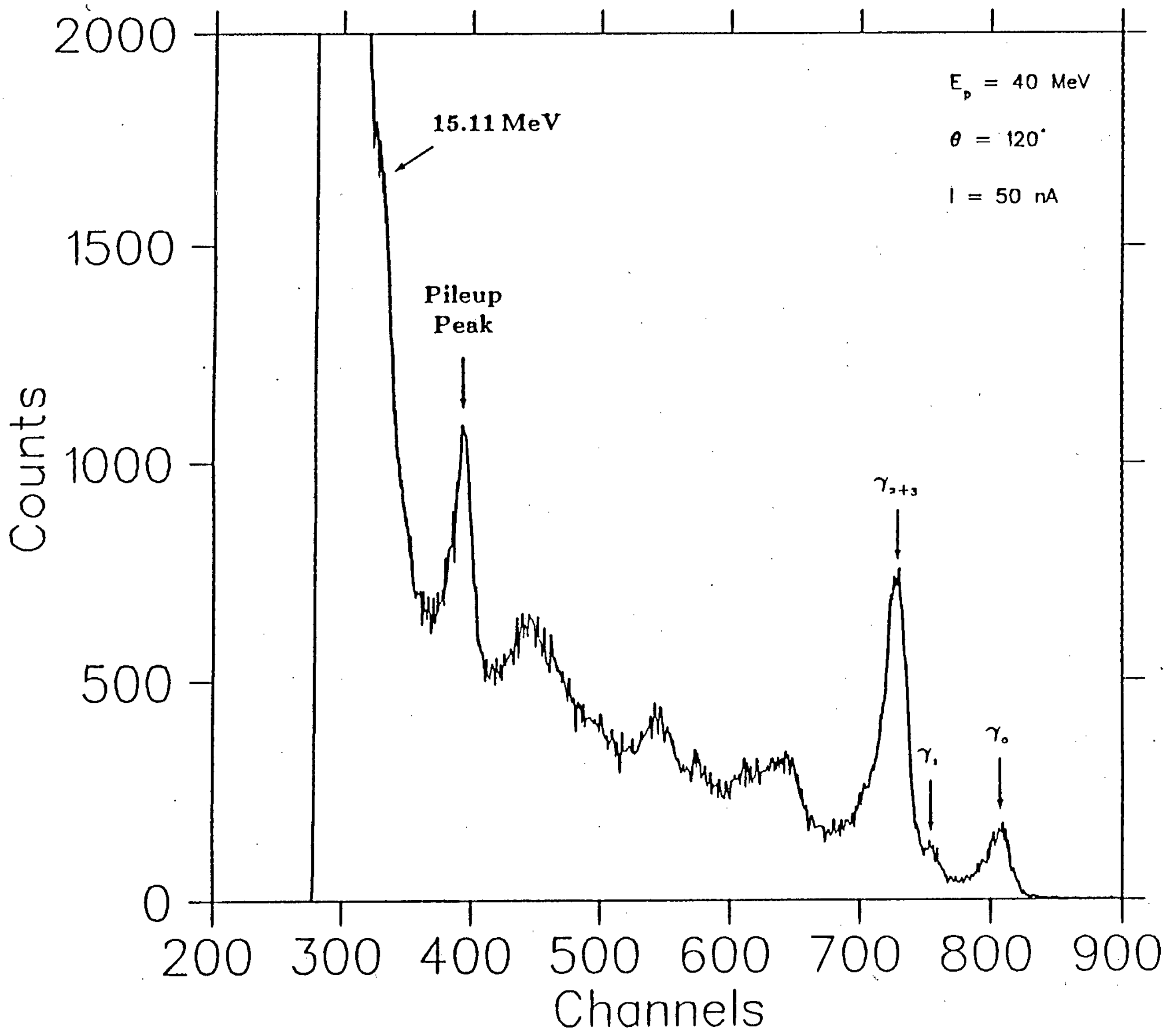

Figure 5.1: A full gamma spectrum taken at 40 MeV showing all features from below the low energy threshold to above the ground state transition.

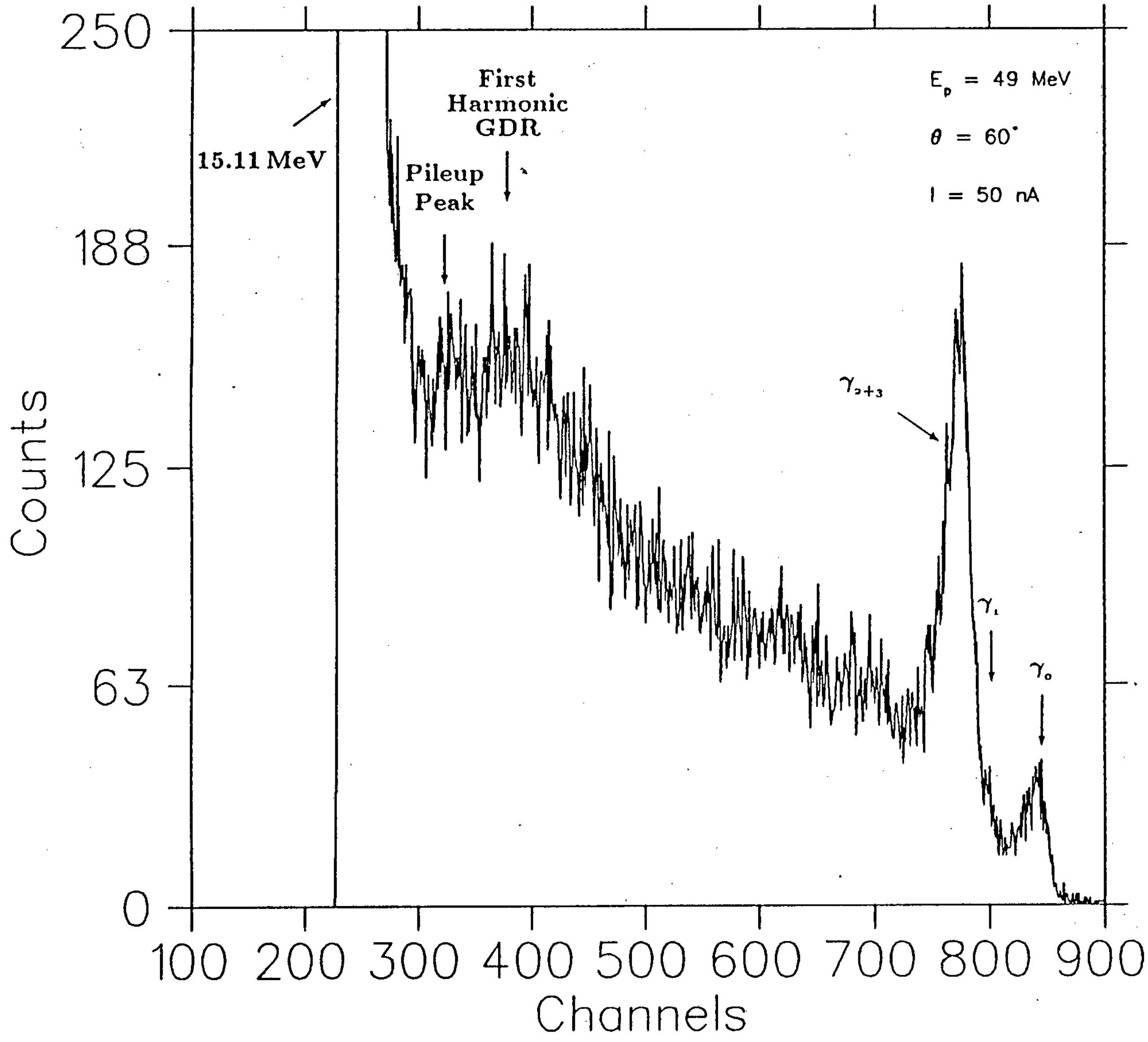

Figure 5.2: A full gamma spectrum taken at 49 MeV showing all features from below the low energy threshold to above the ground state transition.

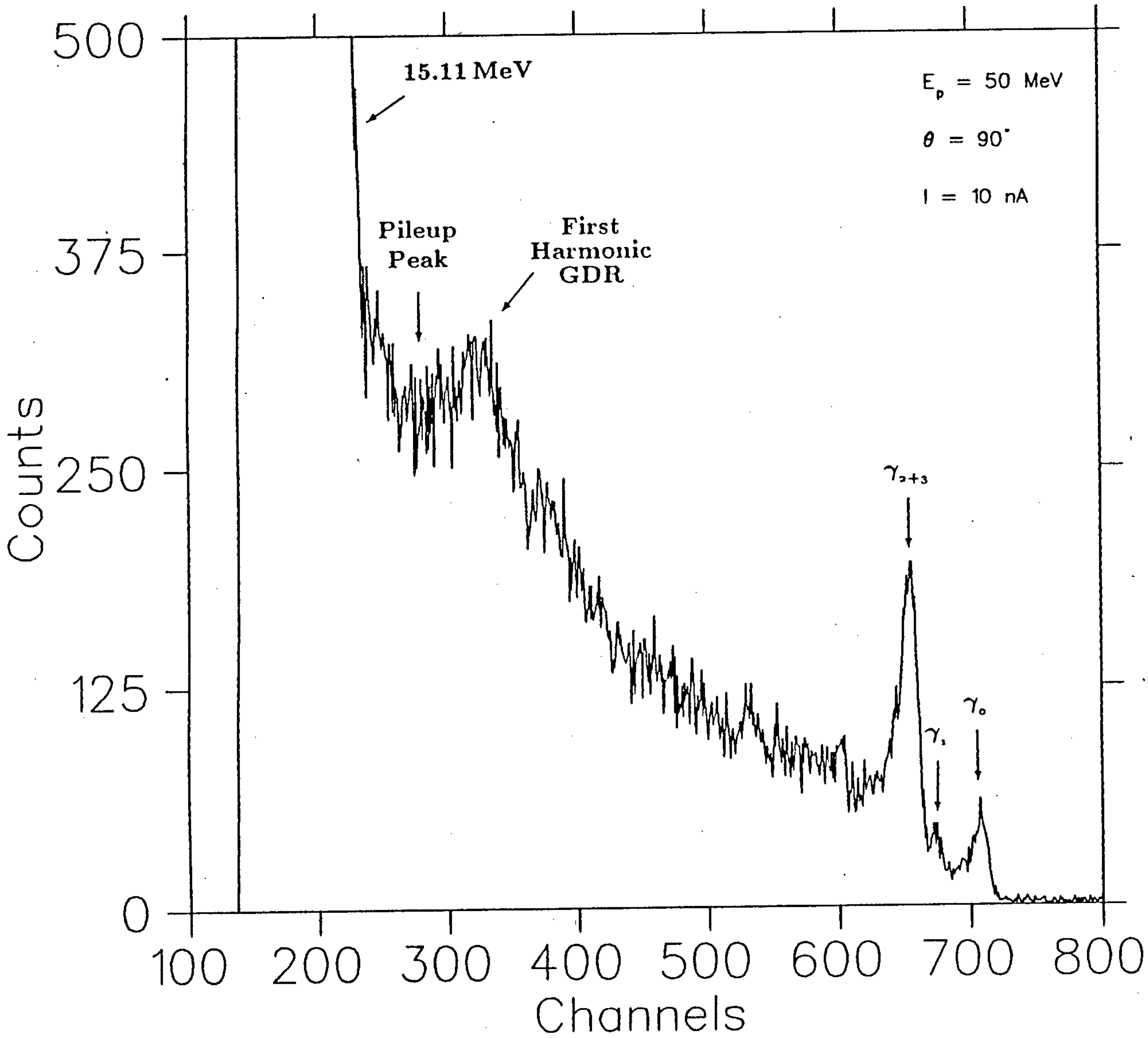

Figure 5.3: A full gamma spectrum taken at 50 MeV showing all features from below the low energy threshold to above the ground state transition.

Bibliography

[Angh 82] M.Anghinolfi, P.Corvisiero, M.Guaurnone, G.Ricco, M.Sanzone, M.Taiuti and A.Zucchiatti, in Proceedings of the International Workshop "Medium Energy Interactions in Nuclear Physics", Pavia (1982) unpublished.

[Berg 76] D.Berghofer, M.D.Hasinoff, R.Helmer, S.T.Lim, D.F.Measday, and K.Ebisawa, Nucl.Phys. **A263** (1976) 109–130.

[Berm 75] B.L.Berman and S.C.Fultz, Rev. Mod. Phys. **47** (1975) 713–761.

[Blat 84] S.L.Blatt, H.J.Hausman, L.G.Arnold, R.G.Seyler, R.N.Boyd, T.R.Donoghue, P.Koncz, M.A.Kovash, A.D.Bacher, and C.C.Foster, Phys. Rev. C **30** No. 2 (1984) 423–433.

[Both 86] A.H.Botha, H.N.Jungwirth, J.J.Kritzinger, D.Reitmann and S.Schneider, Eleventh Int. Conf. on cyclotrons and their applications, (Tokyo, Oct. 1986) p. 9.

[Brin 55] D.Brink, D.Phil. Thesis, University of Oxford (1955) unpublished.

[Corv 81] P.Corvisiero, M.Taiuti, A.Zucchiatti and M.Anghinolfi, Nucl. Instr. and Meth. **185** (1981) 291.

[Fearick] R.Fearick, private communication.

[Ferr 76] S.Ferroni, G.Ricco, G.A.Rottigni, M.Sanzone, and G.Lo Bianco, Il Nuovo Cimento, **35A**, No. 1 (1976) 15.

[Fish 63] P.S.Fisher, D.F.Measday, F.A.Nikolaev, A.Kalmykov and A.B.Clegg, Nucl. Phys. **45** (1963) 113–122.

[Gian 85] M.M.Giannini and G.Ricco, Riv. Nuovo Cim. **8**, No. 4 (1985) 1.

[Gold 48] M.Goldhaber and E.Teller, Phys. Rev. **74** (1948) 1046.

[Goul 81] C.R.Gould, L.G.Holzsweig, S.E.King, Y.C.Lau, R.V.Poore, N.R.Roberson and S.A.Wender, IEEE Trans. Nucl. Sci. **NS-28** No. 5 (1981) 3708.

[Goul 83] C.R.Gould and N.R.Roberson, IEEE Trans. Nucl. Sci. **NS-30** No. 5 (1983) 3758.

[Haus 88] H.J.Hausman, S.L.Blatt, T.R.Donoghue, J.Kalen, W.Kim, D.G.Marchlenski, T.W.Rackers, P.Schmalbrock, M.A.Kovash and A.D.Bacher, Phys. Rev. C **37** No. 2 (1988) 503–511.

[IUCF 84] Indiana University Cyclotron Facility Scientific and Technical Report (1984) 165.

[Jame 75] F.James and M.Roos, Computer Physics Communications **10** (1975) 343–367.

[Meas 73] D.F.Measday, M.Hasinoff and D.L.Johnson, Can. J. Phys. **51** (1973) 1227–1237.

[Myer 74] W.D.Myers and W.J.Swiatecki, Ann. Phys. N.Y. **84** (1974) 186.

[Ohmo 87] C.Ohmori, N.Horikawa, T.Iwata, T.Nakanishi, S.Sakanaka, T.Toyama, K.Hashimoto, T.Murayama, S.Seki and Y.Tagishi, Nucl. Instr. and Meth. **A256** (1987) 361.

[Pilc 89] J.V.Pilcher, Ph.D Thesis, University of Cape Town (1989) unpublished.

[Pühl 77] F.Pühlhofer, Nucl. Phys. **A280** (1977) 267–284.

[Taiu 83] M.Taiuti, M.Anghinolfi, P.Corvisiero, G.Ricco and A.Zucchiatti, Nucl. Instr. and Meth. **211** (1983) 135.

[Well 82] H.R.Weller, H.Hasan, S.Manglos, G.Mitev, N.R.Roberson, S.L.Blatt, H.J.Hausman, R.G.Seyler, R.N.Boyd, T.R.Donoghue, M.A.Kovash, A.D.Bacher and C.C.Foster, Phys. Rev. C **25** No. 6 (1982) 2921–2934

[Woud 87] A. van der Woude, Prog. Part. Nucl. Phys. **18** (1987) 217–293.

[Zucc 86] A.Zucchiatti and J.P.F.Sellschop, S.Afr.J.Phys. **9** (1986) 24.

[Zucc 88] A.Zucchiatti, Ph.D. Thesis, University of the Witwatersrand (1988) unpublished.